Correspondence to:
N. Sakaeda,
nsakaeda@ou.edu

The Unique Characteristics and Potential Mechanisms of the MJO-QBO Relationship

Naoko Sakaeda[1] , **Juliana Dias[2]** , and **George N. Kiladis[2]**

[1]School of Meteorology, University of Oklahoma, Norman, OK, USA, [2]Physical Sciences Laboratory, NOAA, Boulder CO, USA

Abstract Previous studies have shown that Madden-Julian oscillation (MJO) convective activity increases when quasi-biennial oscillation (QBO) easterlies appear in the lower stratosphere, and that this relationship is seen only during boreal winter. However, the physical mechanism behind this relationship is not fully understood. Building upon previous literature on the MJO-QBO relationship, this study first tests whether the relationship between the QBO and MJO extends to other modes of organized tropical convection. Our analysis shows that the QBO does not have any significant relationship with other modes of variability such as convectively coupled equatorial waves (CCEWs). An extended analysis for periods prior to 1979 also shows that the boreal winter QBO-MJO relationship substantially weakens prior to 1979. These results imply that, in addition to the seasonal dependence, any proposed mechanisms for the relationship between the QBO and MJO must be able to explain the uniqueness of this relationship with respect to other CCEWs, as well as the reason for its strengthening after 1979. Among the analyzed modes of tropical convection, the MJO is the most sensitive to the modulation of high cloud fraction and associated radiative feedback by the QBO and this sensitivity may weaken prior to 1979. These results indicate that the strong top-heaviness of vertical motion and cloud-radiative feedback associated with the MJO are important to explain its unique relationship with the QBO.

1. Introduction

Internal atmospheric variability within the tropical trosposphere and stratosphere such as the quasi-biennial oscillation (QBO, Baldwin et al., 2001) and the Madden-Julian oscillation (MJO, Madden & Julian, 1994) are known to provide predictability on seasonal to subseasonal time scales (Boer & Hamilton, 2008; Butler et al., 2019; Marshall & Scaife, 2009). Recently, several studies have found a significant relationship between the MJO and QBO during the boreal winter (Densmore et al., 2019; Hendon & Abhik, 2018; Nishimoto & Yoden, 2017; Son et al., 2017; Yoo & Son, 2016). This relationship provides an additional pathway for sources of predictability on seasonal to subseasonal time scales (Lim et al., 2019; Liu et al., 2014; Marshall et al., 2017). However, it is a major challenge to exploit this source because current general circulation models (GCM) often struggle to simulate both the MJO and QBO (Jiang et al., 2015; H. Kim et al., 2020; Scaife et al., 2014) and the physical mechanism behind their relationship is not well understood. Previous studies show that the QBO-MJO relationship is peculiar for the following reasons: (i) it is only observed during boreal winter (Densmore et al., 2019; Hendon & Abhik, 2018; Nishimoto & Yoden, 2017; Son et al., 2017; Yoo & Son, 2016), (ii) an analogous relationship between the QBO and other modes of tropical variability, such as convectively coupled equatorial waves (CCEWs), is less clear (Abhik et al., 2019), and (iii) the relationship only appears after around 1980 (Klotzbach et al., 2019). Therefore, it is crucial for any hypothesis on the dynamical mechanism underlying the MJO-QBO relationship to be able to explain this particular behavior. The first objective of this study is to reexamine the particular behavior of the QBO-MJO relationship listed above (i–iii) using different methods. The second objective is to identify a potential mechanism that explains the QBO-MJO relationship, as well as its unique behavior.

The QBO is the dominant mode of stratospheric interannual variability in the tropics and is characterized by the downward propagation of alternating easterly and westerly equatorial zonal winds, having a period of about 28 months (Baldwin et al., 2001). The fundamental dynamics of the QBO is governed by the vertical transport of momentum by equatorial stratospheric waves, which can be triggered by convection (Fritts & Alexander, 2003; Geller et al., 2016; Nishimoto et al., 2016). At the same time, changes in the circulation and temperature associated with the QBO can also influence tropical convection, including the MJO

(Collimore et al., 2003; Gray et al., 1992; Lee et al., 2019; Liess & Geller, 2012; Nie & Sobel, 2015; Taguchi, 2010).

The MJO is the dominant mode of tropical intraseasonal variability, which is characterized by eastward propagating, planetary scale envelopes of anomalous convection (Madden & Julian, 1994; C. Zhang, 2005). MJO amplitude tends to be larger during QBO lower stratosphere easterlies and weaker during QBO westerlies, and, as mentioned above, this relationship exists exclusively during the boreal winter (Hendon & Abhik, 2018; Nishimoto & Yoden, 2017; Son et al., 2017; Yoo & Son, 2016; Zhang & Zhang, 2018). Some studies suggest that the overall greater amplitude of the MJO during the QBO easterly results from an increased duration and number of MJO events, rather than an intensification of each event (Nishimoto & Yoden, 2017; Zhang & Zhang, 2018). These previous studies have suggested that the QBO influences the MJO through modulations of the upper-tropospheric temperature and static stability, tropopause height, or associated changes in high cloud fraction and its radiative feedback (Hendon & Abhik, 2018; Martin et al., 2019; Nishimoto & Yoden, 2017; Son et al., 2017; Yoo & Son, 2016; Zhang & Zhang, 2018). QBO easterlies in the lower stratosphere are accompanied by negative temperature anomalies below to maintain thermal wind balance, leading to decreased static stability in the upper troposphere. Hendon and Abhik (2018) suggested that the upper-tropospheric negative temperature anomalies associated with the MJO aids the destabilization induced by the QBO, leading to a strengthening of the MJO during the QBO easterlies. The impact of the QBO on MJO convection is strongest over the Maritime Continent and western Pacific basin, which was suggested to occur due to increased durations of MJO convection and eastward propagation speeds across the Maritime Continent (Densmore et al., 2019; Hendon & Abhik, 2018; Son et al., 2017; Zhang & Zhang, 2018).

Most of the previously hypothesized mechanisms of the QBO-MJO relationship are not necessarily exclusive to the MJO. For example, it is not clear why the upper tropospheric destabilization leads to increased in MJO convection amplitude but not other convective modes. However, Abhik et al. (2019) recently showed that the QBO appears to have no significant relationship with other modes of tropical convection. An exception appears with convectively coupled Kelvin wave during the boreal spring, where its activity weakly increases during QBO easterlies. Abhik et al. (2019) attributed this weaker QBO-Kelvin relationship to differences in the vertical profile of temperature anomalies associated with the Kelvin waves and MJO. Their vertical profiles of temperature anomalies both show anomalous cooling in the upper troposphere. This anomalous cooling results in additional destabilization at the upper troposphere, but the more pronounced vertical tilt in the temperature profile of Kelvin wave leads to a displacement of the destabilization from the center of Kelvin wave convection, resulting in its weaker relationship with the QBO. Although the results of Abhik et al. (2019) suggest the importance of differences in vertical profiles of the MJO and Kelvin waves, other CCEWs also tend to induce thermal destabilization in the upper troposphere and it is not clear why the QBO does not have significant relationships with other CCEWs.

A number of studies suggest that the MJO and CCEWs have distinct dynamics and growth mechanisms, which are supported by differences in their thermodynamic and dynamic profiles and relationship with moisture (e.g., Adames et al., 2019; Inoue et al., 2020; Raymond & Fuchs, 2007; Sakaeda et al., 2020; Sobel et al., 2001; Yasunaga & Mapes, 2011, 2013). Adames et al. (2019) suggest that the more slowly propagating waves such as the MJO and equatorial Rossby (ER) waves behave more like moisture modes, where the weak temperature gradient (WTG) approximation (Sobel et al., 2001) is more applicable to its dynamics, the temperature fluctuations are more fundamental to faster-propagating waves such as Kelvin and inertio gravity waves. Under the WTG assumption, the static stability impacts the sensitivity of vertical motions that arise in response to diabatic heating (Chikira, 2014; Wolding et al., 2016, 2017). If one hypothesizes that such a mechanism is responsible for modulating the strength of tropical convection, then we expect the QBO to influence any tropical convective mode whose fundamental dynamics still operates under the WTG approximation such as the ER wave (Adames et al., 2019; Bretherton & Sobel, 2003), and it does not explain the exclusive relationship between the QBO and MJO. Therefore, further comparison of QBO relationships with various modes of tropical convection may help us understand the mechanism underlying the unique QBO-MJO relationship. This study first reexamines the results of Abhik et al. (2019) and Klotzbach et al. (2019) to confirm the unique relationship between the QBO and MJO and its exclusive appearance after 1979 using different analysis techniques. We will then discuss potential mechanisms underlying the QBO-MJO relationship.

2. Data and Methods

2.1. QBO Index and Reanalysis Data

To diagnose the state of the QBO, this study uses zonal-mean monthly 50 hPa zonal wind from the JRA-55 reanalysis from Japan Meteorological Agency (JMA) (Kobayashi et al., 2015) from 1958 to 2017, averaged from 10°S to 10°N. The seasonal cycle is first removed by subtracting the mean and the first three harmonics of the monthly seasonal cycle. The anomaly is then normalized by using its monthly standard deviation for each month of the year. Previous studies have used ECMWF ERA-Interim (ERA-I) reanalysis (Dee et al., 2011) instead of JRA-55 (Nishimoto & Yoden, 2017; Son et al., 2017; Yoo & Son, 2016), but the correlation between the QBO indices using ERAI and JRA is 0.99 between 1979 and 2017. This index is referred to as the QBO index throughout the manuscript.

JRA-55 reanalysis data on 2.5° × 2.5° horizontal resolution is also used to examine the atmospheric profiles associated with the QBO and wave modes (MJO and CCEWs). While the atmospheric profiles of the QBO is examined using monthly data, 6-hourly resolution is used to examine the wave modes. The same analysis was repeated using ERA-I and our conclusion is not sensitive to the choice of reanalysis data. Our analysis mainly focuses on the period between 1979 and 2017 when the satellite data are available, but we also present results with JRA-55 data that extends back to 1958. We also use JRA-55C, which does not assimilate satellite observations and only uses conventional surface and upper air observation. JRA-55C is available from November 1972 to December 2012. Comparison of JRA-55 with JRA-55C shows impacts of assimilating satellite observations on our results.

2.2. Convective Activity

This study uses interpolated Outgoing Longwave Radiation (OLR) from NOAA to estimate convective activity (Liebmann & Smith, 1996). These data provide the longest observational record that can be used to estimate convective activity and are available twice daily from 1979 at a 2.5° × 2.5° horizontal resolution. OLR anomalies are calculated by subtracting its mean and the first three harmonics of the seasonal cycle. We have also used CLAUS brightness temperature (Hodges et al., 2000), ISCCP cloud fraction (Rossow & Schiffer, 1999), and TRMM Multisatellite Precipitation Analysis (TMPA) 3B42 rainfall rate Huffman et al. (2007) data to test consistency. General conclusions are insensitive to the choice of data, but the results with OLR data are presented here as it provides the longest record.

2.3. ENSO Index and SST Data

Another interannual mode of variability that is known to influence the activity of the MJO and CCEWs is the El Niño–Southern Oscillation (ENSO). To diagnose and separate the relationship between the ENSO, QBO, and convective activity, we use the monthly oceanic Niño 3.4 index from NOAA Climate Prediction Center smoothed with a 3-month running window. The Niño 3.4 index is generated using NOAA extended reconstructed sea surface temperature (SST) version 4 (B. Huang et al., 2015).

2.4. Correlation and Windowed Fourier Transform Analysis

To examine the relationship between the QBO and CCEWs in section 3, we use the monthly time series of wave number-frequency power spectra calculated following the method of Wheeler and Kiladis (1999), which applies Fourier transforms to global OLR anomalies 15°N to 15°S with a 96-day window that is centered on the 15th day of each month. For each window, a temporal linear trend is removed and the beginning and ending 10% of the OLR anomalies are tapered to zero using a Hanning window. The 96 day window is chosen to be long enough to capture subseasonal convective activity. The monthly time series of these power spectra is then correlated with the monthly QBO index. For this component of the analysis, a 3-month running mean is applied to the QBO index to match the window of the seasonal (96-day) power spectrum. The power spectra are calculated for symmetric and antisymmetric components about the equator and correlated with the QBO index.

Since MJO and CCEW activity is known to be influenced by ENSO (Hendon et al., 2007; P. Huang & Huang, 2011; Kessler, 2001), we reduce its impact by removing signals of the power spectral coefficients that are linearly associated with Niño 3.4 index. To do so, the monthly time series of power spectra is regressed onto Niño 3.4 index, and the resultant regression coefficients are used to reconstruct and remove the variability associated with ENSO. We use this technique to minimize ENSO signals throughout our analysis.

Table 1

Wave Number and Frequency Filtering Band for the MJO and CCEWs, Where k is the Planetary Zonal Wave Number, ν the Frequency in Cycles per Day, and h_{eq} the Equivalent Depth in Meters

Mode	k	ν	h_{eq}
MJO	0 to 8	1/96 to 1/30	—
Kelvin	1 to 15	1/17 to 1/2.5	8–90
Equatorial Rossby (ER)	−10 to −1	1/96 to 1/10	1–90
Westward inertio gravity (WIG)	−15 to −1	0.3–0.8	8–90
Eastward inertio gravity (EIG)	0 to 15	0.2–0.55	12—90
Mixed Rossby gravity (MRG)	−10 to −1	—	8—90
Tropical disturbance (TD)	−15 to −5	0.2–0.8	—
Eastward high frequency	1 to 30	0.5–1	—

Note. Positive k corresponds to eastward propagation and negative k corresponds to westward propagation of the mode.

Figure 1. (a) An example of wave phase diagram defined by the normalized time series of wave-filtered OLR (OLR_{wave}) and its time tendency ($dOLR_{waves}/dt$). The angles show the defined wave phase (λ). (b) Composite of wave-filtered OLR based on the wave phase.

Furthermore, linear trends from the entire period are removed from each data set before any regression or correlation analysis is applied.

2.5. Evaluation of Wave Activity and Structure

To assess geographical variability of the QBO impacts, we filter OLR anomalies for the MJO and CCEWs using the inverse Fourier transform technique by Wheeler et al. (2000), except that symmetric or antisymmetric components were not specified. Wave number-frequency bands that are used to filter for all the waves are summarized in Table 1. The monthly variance of these filtered OLR anomalies is then calculated at each grid point, which generates monthly time series of convective activity for each wave mode. This monthly time series of the wave variance is correlated or composited using the QBO and ENSO indices to examine their relationships. Small changes to the selection of filtering parameters do not influence the conclusions of this study.

We evaluate the vertical structure of the wave modes using wave phase diagram (Figure 1) in section 5.1, which has been used by previous studies (Riley et al., 2011; Sakaeda et al., 2020; Yasunaga & Mapes, 2011). The wave phase is defined by the 12-hourly time series of wave-filtered OLR and its time tendency. Both time series are standardized by their seasonal standard deviation within the entire tropics between 15°N and 15°S. The amplitude of the wave phase is calculated as the square root of the sum of the squared time series. We only include time and points above an amplitude of one, so the sampling is geographically skewed toward convectively active regions of each wave. Wave phases at 0° and ±180° indicate the centers of enhanced and suppressed convective envelopes, respectively. The state where the convection is amplifying or approaching is indicated by negative wave phase angles and the state of decaying convection is indicated by positive wave phase angle.

2.6. Statistical Significance Test

Statistical significance of all analyses in this study is tested using a bootstrap resampling test of 1,000 iterations of the same sample size. This bootstrap test is used to generate a distribution of correlation coefficients, which is tested against a noise distribution. The noise distribution is generated by repeating the same correlation analysis while reversing the temporal sequence of one of the time series, which allows us to generate the noise distribution with data that has the same autocorrelation characteristics. The correlation coefficients are determined to be statistically significantly different from zero when the confidence interval of the bootstrap resampling distribution does not overlap with the confidence interval of the noise distribution. This method is similar to the statistical significance test done for cross spectral analysis in Dias & Kiladis (2016) and Sakaeda et al. (2017). The bootstrap test is also used for composite analysis where composite values are determined to be statistically significantly different from zero when the confidence interval is above or below zero. A confidence level of 95% for statistical significance is used throughout this study. Similar statistical significance results were obtained using the Student's t-test on our correlation analysis
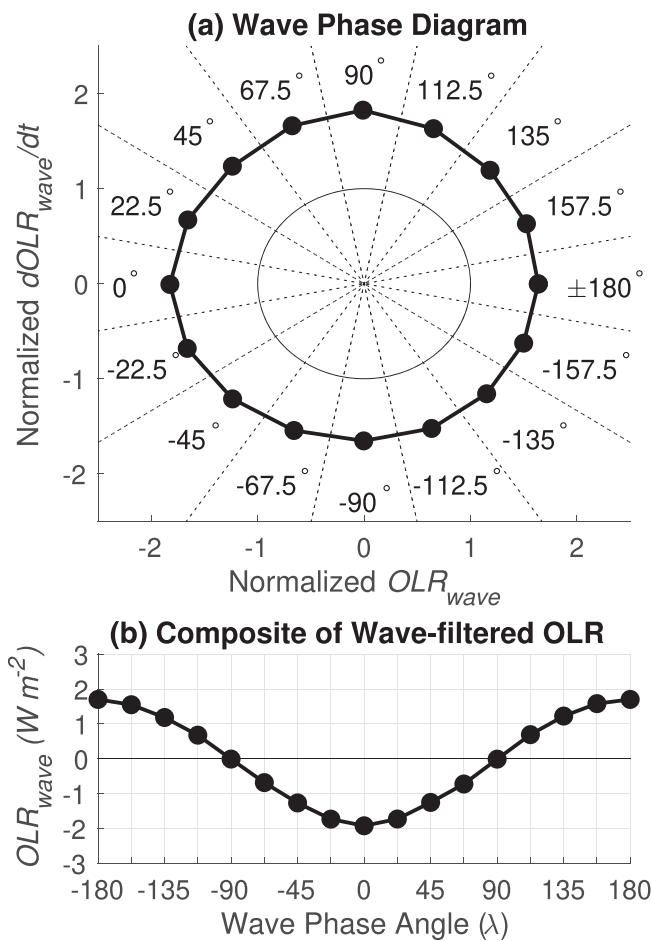
with the number of years (38 years) as the degrees of freedom. We will present results with the bootstrap test for consistency among different analysis techniques that we use.

3. Relationship Between the QBO and CCEWs

In this section, we first reevaluate the results of Abhik et al. (2019) on the relationship between the QBO and CCEWs. Figure 2 shows the correlation coefficients between monthly symmetric and antisymmetric power spectra of OLR anomalies and the QBO index for each season. The monthly time series of the OLR spectra were calculated using the method described in section 2.4. The correlation during DJF is calculated by using the power spectrum centered on the 15th day of December, January, and February, and similarly, for the correlations during the other three seasons. Negative correlations indicate that the OLR variance at a particular frequency and wave number is enhanced during QBO easterlies and vice versa.

Figures 2a and 2b show that significant negative correlations appear over the MJO band in both the symmetric and antisymmetric components and only during boreal winter, as shown in previous studies (Abhik et al., 2019; Nishimoto & Yoden, 2017; Son et al., 2017; Yoo & Son, 2016). During boreal winter, positive correlations appear around the westward inertio gravity (WIG) wave number-frequency band, which indicates a suppression of its activity during QBO easterlies. Some enhancement of convective activity around the eastward inertio gravity (EIG) band also occurs during the easterly QBO in DJF and MAM. These relationships between the QBO and inertio gravity waves were not detected by Abhik et al. (2019), perhaps because they examined the relationship by comparing the composites of power spectra. Since the power is small at higher frequencies, it is difficult to detect its small changes with the QBO. During SON, ER waves tend to be enhanced in QBO easterlies as also shown by Abhik et al. (2019). Figure 2c also shows weakly negative (but not statistically significant) correlations between the QBO index and OLR power spectra around the Kelvin wave band during MAM, suggesting slightly stronger Kelvin waves with QBO easterlies as shown by Abhik et al. (2019).

While the power spectrum captures the integrated activity of CCEWs in the entire tropics, their activity is geographically nonuniform (Dias & Kiladis, 2014; Kiladis et al., 2009; Roundy & Frank, 2004). To evaluate spatial inhomogeneity in the relationship between the QBO and CCEWs, we mapped the correlation coefficients between the monthly QBO index and monthly variance of filtered OLR anomalies at each grid point for each wave (not shown), including the tropical depression waves (TD, Roundy & Frank, 2004; Wheeler & Kiladis, 1999) band and eastward propagating, high-frequency band that showed some correlation with the QBO (defined in Table 1 and Figured 2a and 2b). This analysis found weak, but not significant correlations for the TD and high-frequency eastward disturbance throughout most of the tropics, leading to a significant correlation when the wave activity is integrated over the entire tropics in the power spectrum analysis. However, the MJO is the only mode that shows statistically significant correlations with the QBO when it is examined on a map view. Therefore, consideration of spatial inhomogeneity in the wave activity supports the view that the QBO influences the MJO exclusively during boreal winter.

One contrast between our results with Abhik et al. (2019) is that we do not find a clear relationship between the QBO and Kelvin wave during MAM, even at the 90% confidence level as shown by Abhik et al. (2019). Although Figure 2c shows a weakly negative correlation, this is not confined to the Kelvin wave band as it is seen in other areas of the space-time spectra. To control for ENSO, this study removes the linear signals associated with Niño 3.4 index whereas Abhik et al. (2019) considered months when the Oceanic Niño Index (ONI) was within ± 0.75. Neither method completely removes the impacts of ENSO on CCEW activity. Figures 3a and 3b show the distributions of two ENSO indices during the QBO easterly and westerly events identified by Abhik et al. (2019) during MAM. A slight skewness in ENSO state remains within ± 0.75 of either ENSO index, where a La Niña state is favored during QBO westerlies and an El Niño state is favored during QBO easterlies. As shown by P. Huang and Huang (2011), Kelvin waves are stronger during El Niño; therefore, any skewness of ENSO conditions during the easterly and westerly QBO phases could be artificially reflected as a weak relationship between the QBO and Kelvin waves.

Figures 3c and 3d show the correlation coefficients between the QBO index and monthly time series of the power spectrum that is constructed as a function of the Niño 3.4 index (P_E') using a linear regression model. P_E' was removed for the correlation analysis shown in Figure 2 to reduce the variability associated with
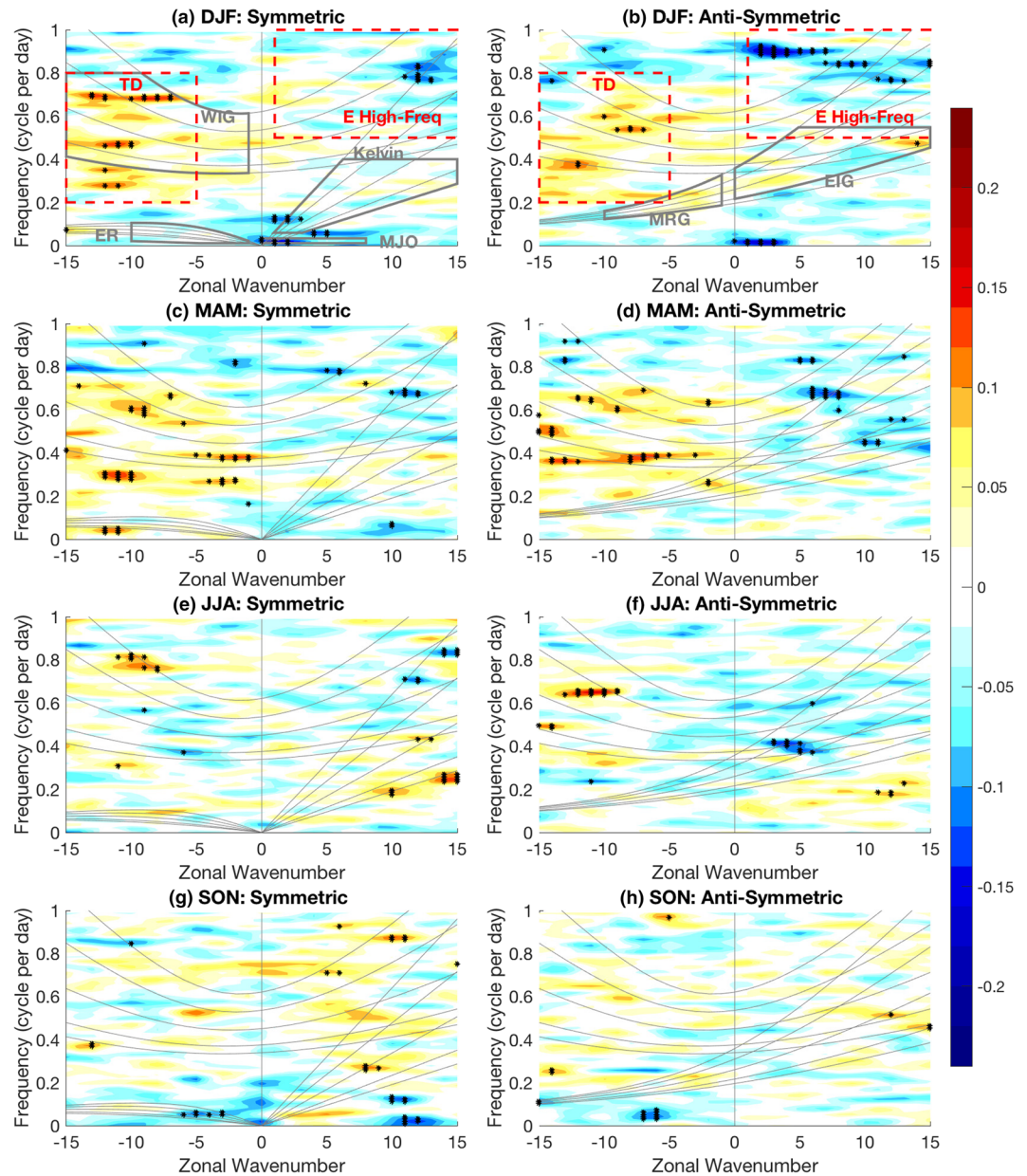
Figure 2. Correlation between the monthly QBO index and wave number frequency power spectral coefficients of OLR anomalies averaged between 15°N and 15°S during each of the four seasons (DJF, MAM, JJA, and SON; see text for more details). Left column (a, c, e, and g) shows the power spectrum of equatorially symmetric component of the OLR anomalies and the right column (b, d, f, and h) shows the antisymmetric component. Black curves show the Matsuno's dispersion curves at the equivalent depths of 8, 12, 25, 50, and 90 m. Black dots indicate the correlation coefficients that are statistically significantly different from zero with the 95% confidence level. Gray and red boxes show the wave number frequency bands used to filter for each mode, as summarized in Table 1. The correlation coefficients are smoothed in both the wave number and frequency directions using 1-2-1 weighting.

ENSO. The correlation between P'_E and the QBO represents the apparent relationship between the QBO and power spectrum that results from the QBO-ENSO relationship (Figured 3a and 3b), not from the direct relationship between the QBO and spectrum. The negative correlations at the Kelvin wave band demonstrate the artifact of ENSO on the apparent relationship between the QBO and OLR. This ENSO artifact still appears even when the correlation between the QBO and P'_E is calculated using years when ENSO indices
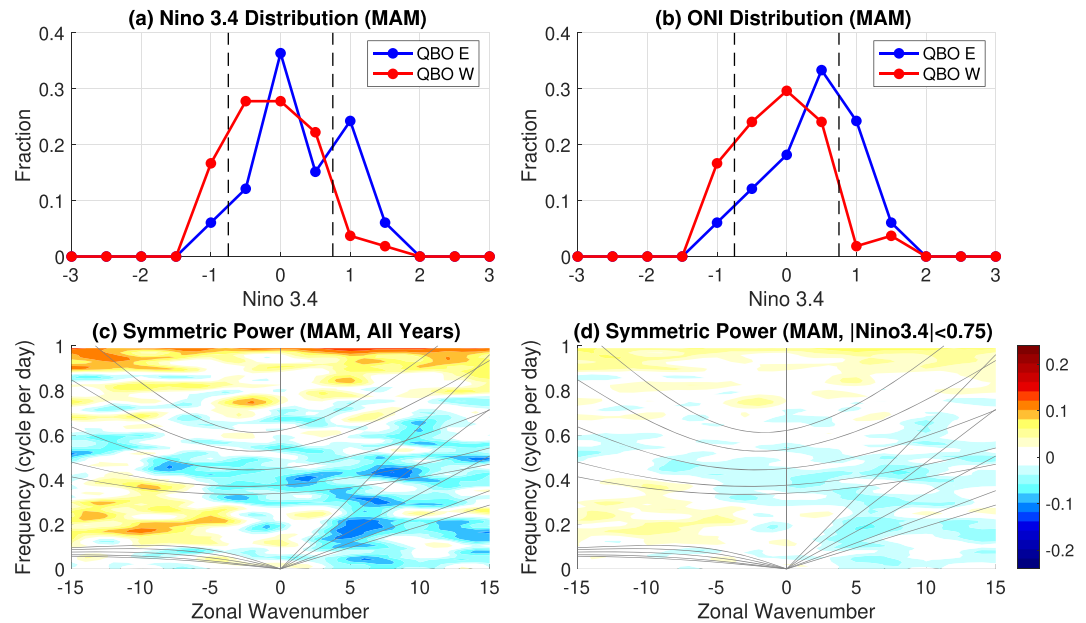
Figure 3. (a) Distribution of Niño 3.4 index during the March-April-May (MAM) QBO easterly and westerly events identified by Abhik et al. (2019). (b) Same as (a) except showing the distribution of ONI. (c) Same as Figure 2c except showing the correlation with the monthly time series of power spectral coefficients that are constructed as a linear function of Niño 3.4 index. (d) Same as (c) except that the correlation coefficients are calculated using the months when Niño 3.4 index was within $\pm$0.75.

were within $\pm$0.75 (Figure 3d). We have also examined the ENSO influence through composite analysis as done by Abhik et al. (2019). The ratio of Kelvin wave average power between QBO easterly and westerly events is 1.12, which is a similar number to what was found by Abhik et al. (2019). However, we do not find this number to be statistically significantly different from one at the 90% confidence level. Furthermore, this ratio reduces to 1.09 when a linear-ENSO signal is removed from the monthly time series of the power spectrum.

Our analysis generally confirms the conclusions by Abhik et al. (2019) that the MJO is the only mode that has statistically significant relationship with the QBO at high confidence level (i.e., 95%), which only occurs during DJF. No statistically significant relationship was found between the CCEWs and monthly zonal equatorial wind at any pressure levels in the stratosphere, even when we considered time lags. Therefore, we conclude that results of the weak Kelvin-QBO relationship by Abhik et al. (2019) are not statistically stable in our analysis. These results suggest caution when examining the combined effects of the QBO and ENSO on the activity of waves.

4. Combined Effects of the QBO and ENSO on the MJO and CCEW Activity

While there is not a significant linear relationship between the QBO and ENSO (Collimore et al., 2003; Liess & Geller, 2012; Xu, 1992), some previous studies have documented a nonlinear relationship between the ENSO and QBO (Geller et al., 2016; Schirber, 2015; Taguchi, 2010). The nonlinear relationship is expected because the QBO is primarily driven by equatorial stratospheric waves that are initiated by tropical convection. Therefore, the amplitude, periodicity, and downward propagation speed of the QBO can be influenced by the changes in tropical convective activity associated with ENSO. In this section, potential nonlinear effects of the QBO and ENSO are considered by examining how the variance of wave-filtered OLR anomalies changes as a function of both the QBO and ENSO. The left column of Figure 4 shows the relationship of QBO and ENSO events during each season. The numbers and shading indicate how many samples (months) had different combinations of QBO and Niño 3.4 indices. During DJF, negative Niño 3.4 values occur preferentially during the easterly QBO months, but the Niño 3.4 values are more uniformly spread during westerly
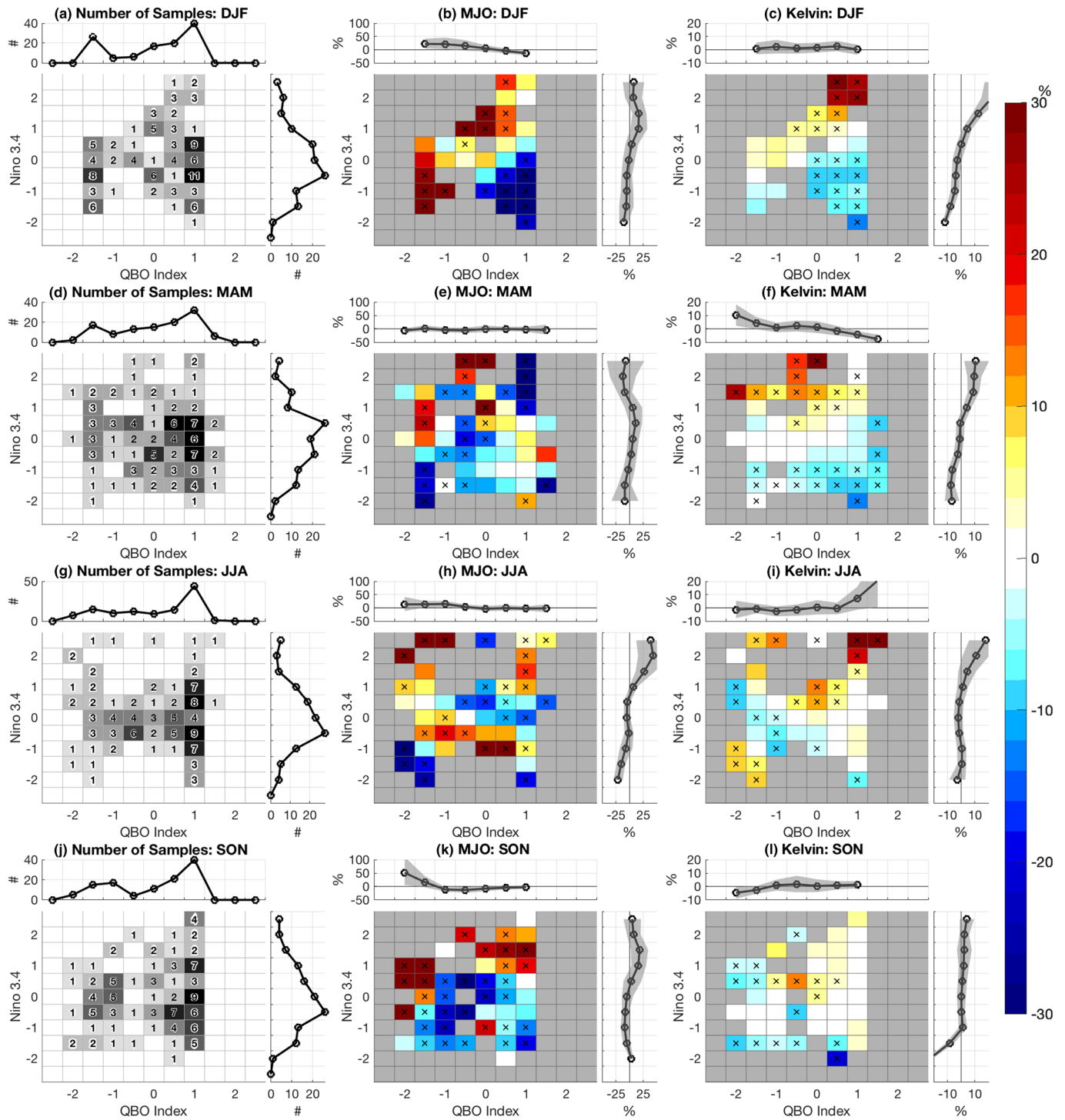
Figure 4. (Left column) Joint distribution of the number of events by QBO and Niño 3.4 indices during (a) DJF, (d) MAM, (g) JJA, and (j) SON. The numbers within each box indicate the number of months that fall within the QBO and Niño 3.4 index bins. Both indices are normalized by its seasonal standard deviation. The horizontal line on the top shows the distribution of samples by QBO index only and the vertical line on the right shows the distribution of samples by Niño 3.4 index only. (Middle column: b, e, h, k) Shading shows the mean normalized anomalous variance of MJO-filtered OLR at each QBO and Niño 3.4 bins for each season (see Equation 1). Crosses indicate anomalies that are statistically significantly different from zero at the 95% confidence level. The horizontal line on the top of these panels shows the mean normalized variance anomalies of MJO-filtered OLR based on the QBO index, and the vertical line on the right shows the mean normalized variance anomalies based on Niño 3.4 index with their 95% confidence interval indicated with gray shading. (Right column: c, f, i, l) Same as the middle column, except for Kelvin wave.

QBO months (Figure 4a). This nonlinear relationship between ENSO and QBO is most robust during DJF, but is observed in other seasons (Figures 4d, 4g, and 4j), particularly in SON.

The middle and right columns of Figure 4 show normalized anomalous variance of filtered OLR anomalies for the MJO and Kelvin wave binned as a function of both QBO and ENSO indices for each season. For each combination of QBO and Niño 3.4 index, area-weighted average of monthly variances of filtered OLR anomalies over the tropics (15°S to 15°N) are calculated to generate tropical-mean variances $\sigma(k, l)$, where k is the QBO index and l is the Niño 3.4 index. The normalized anomalous variance is then calculated as

$$\sigma^{'}(k, l) = 100 \times (\sigma(k, l) - \overline{\sigma})/\overline{\sigma} \tag{1}$$

where σ is the climatological variance of the filtered OLR anomalies during each season. The horizontal and vertical lines on the top and right show the normalized anomalous variance as a function of QBO or Niño 3.4 index ($\sigma'(k), \sigma'(l)$). These normalized anomalies provide a concise view of how the convective activity of each mode changes as a function of both the QBO and ENSO.

Statistical significance of the normalized anomalous variance is tested using bootstrap resampling. The anomalous variance (σ') is considered statistically significantly different from zero if the 95% confidence interval of σ distribution is above or below the 95% confidence interval of σ. As shown in the left column of Figure 4, some bins only have one sample, for which the distribution cannot be generated. In this case, σ' is considered to be statistically significant if σ is above or below the 95% confidence interval of σ. This method was chosen to provide some guidance on the degree of deviation of the anomalies from the climatology, yet it should be recognized that the resultant statistical significance test can be sensitive to small changes in the sample size.

Figure 4b shows that MJO convective activity during DJF can vary as a function of both the QBO and ENSO. During QBO westerlies, the global variance of MJO convection is higher during ENSO warm phases. During neutral and cold ENSO phases, the MJO variance increases from the QBO westerlies to easterlies, contributing to the observed relationship between the MJO and QBO. This result suggests that the observed relationship between the MJO and QBO is not entirely related to ENSO. However, the lack of samples with a combination of easterly QBO and warm ENSO state makes it difficult to conclude whether the appearance of the observed relationship between the MJO and QBO is conditioned by ENSO. This result also suggests that the lack of relationship between the global MJO activity and ENSO found by previous studies (e.g., Hendon et al., 2007) is due to the spread in the MJO activity associated with the QBO. During other seasons (Figures 4e, 4h, and 4k), the relationship between the MJO and QBO does not appear.

In contrast to the MJO, Kelvin waves appear to be more sensitive to the state of ENSO than the QBO, especially during DJF and MAM. This result again indicates that the weak QBO-Kelvin relationship during MAM in Abhik et al. (2019) could be due to ENSO. Other modes of tropical convective activity also appear to be more sensitive to the state of ENSO than the QBO during DJF, except for MRG and ER wave activity, which does not seem to depend on either (not shown). These results further confirm that the QBO has the strongest relationship with the MJO during DJF, and its relationship with other modes of tropical convection is weak throughout the year.

4.1. Analysis of the QBO-MJO Relationship in the Historically Extended Period

Recently, Klotzbach et al. (2019) suggested that the QBO-MJO relationship only appears after around 1980 due to the reduction of tropopause layer temperature and static stability over time with climate change. In addition to the change in the static stability, Figure 4 suggests that this absence of QBO-MJO relationship before 1980 may be due to differences in the samples of ENSO states, which is examined using JRA-55.

We first use cross-spectral analysis on wave number-frequency domain to check the consistency of JRA-55 OLR with the observed OLR. Figures 5a and 5b show their coherence squared between 1979 and 2017. Coherence is obtained using Fourier transformed coefficients that are calculated following the same method described in section 2.4. The coherence between the observed and JRA-55 OLR is high (above 0.7) for low-frequency time scales such as the MJO and ER wave but decreases to below 0.1 for time scales shorter than 2 days. This low coherence partly results from the lack of high temporal resolution in observed OLR, but the results generally suggest that the discrepancy between observed and JRA-55 OLR increases for
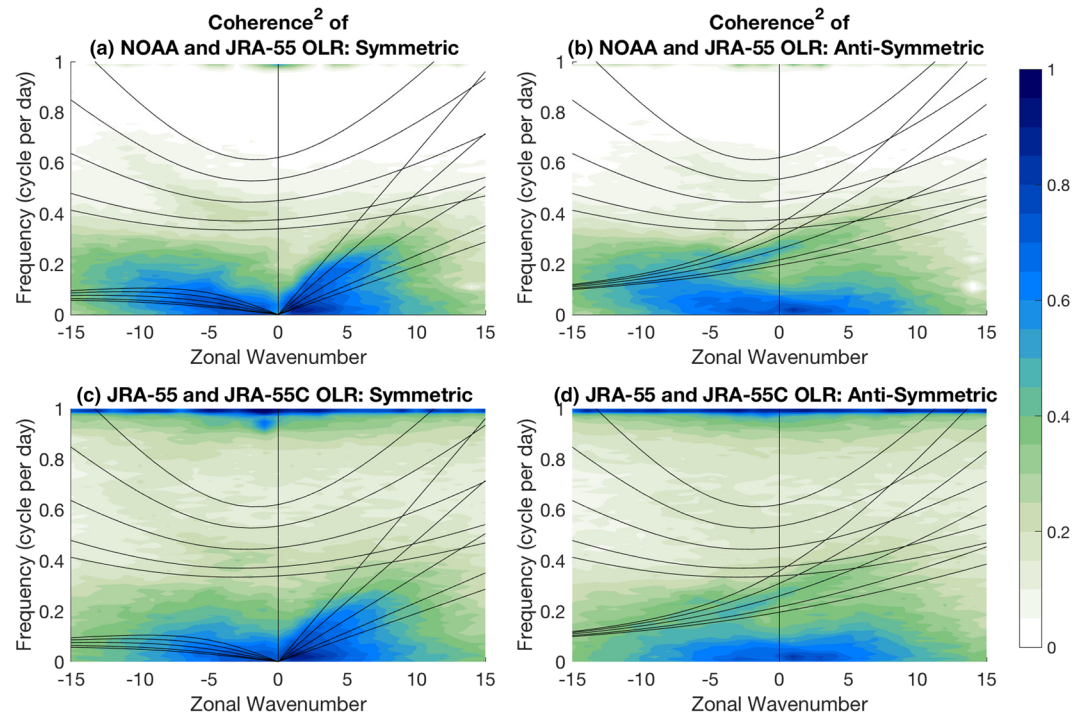
Figure 5. Cross spectral coherence squared of (a, b) NOAA observed OLR and JRA-55 OLR between 1979 and 2017 and (c, d) JRA-55 and JRA-55C OLR between 1973 and 2012. The left column shows symmetric and right column shows antisymmetric components. The coherence was calculated using the Fourier transform coefficients calculated in the same method described in section 2.

higher-frequency CCEWs. JRA-55 OLR is also compared with JRA-55C (Figures 5c and 5d), which still show high coherence of the MJO, indicating that the MJO convective variability is less influenced by the availability of satellite observations. However, the assimilation of satellite data has a greater impact on the higher-frequency variability, indicated by below 0.5 coherence squared on time scales shorter than 10 days. These results suggest the density of sounding data that were available before satellite era provides sufficient data to capture the MJO by JRA-55 prior to 1979; however, the capability of capturing the CCEWs prior to satellite is questionable. Therefore, our analysis prior to 1979 will focus solely on the MJO.

Figure 6b shows that the variance of MJO-filtered OLR from JRA-55 varies with the QBO and ENSO in the same manner as shown with observed OLR in Figure 4b. The same result was obtained using OLR from JRA-55C. When the analysis period is extended to 1958, Figures 6c and 6d show that this historically extended period from 1958 to 1978 fills in the lack of samples in the combination of QBO easterly and El Niño states from 1979 to 2017. The MJO convective activity also shows no apparent relationship with the QBO or ENSO between 1958 and 1978, which eliminates the QBO-MJO relationship when examined from 1958 to 2017 (Figures 6e and 6f). These results show that the absence of QBO-MJO relationship prior to 1979 (Klotzbach et al., 2019) does not occur from the sample differences in ENSO.

5. Hypothesized Reason for the Exclusive QBO-MJO Relationship

This section will first discuss if previously proposed mechanisms can explain the MJO-QBO relationship that appears exclusively with the MJO, during boreal winter only, and after 1979. Then we will propose a new mechanism that may explain this particular relationship.

Previous studies have suggested that the seasonal dependence of the QBO-MJO relationship may be explained by the seasonal cycle of the MJO (Nishimoto & Yoden, 2017; Son et al., 2017; Yoo & Son, 2016). As shown in Figure 7a, MJO convective activity is known to shift into the summer hemisphere and it is strongest during the boreal winter (Roundy & Frank, 2004; Zhang & Dong, 2004). The QBO wind and temperature anomalies decay away from the equator, therefore, northward shift and weakening of MJO
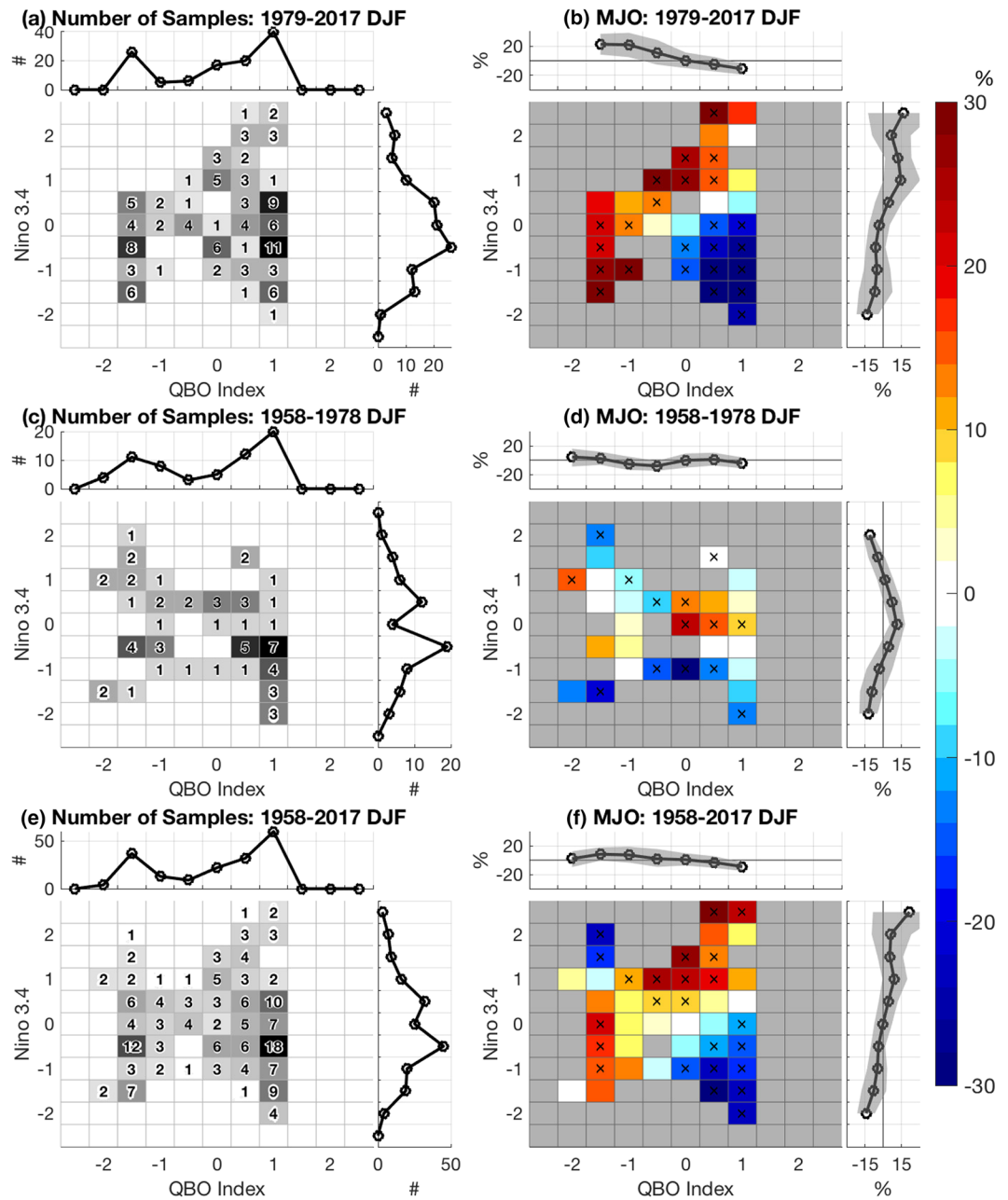
Figure 6. Same as Figures 4a and 4b, except showing the variance of MJO-filtered OLR from JRA55 during DJF during (top row) 1979–2017, (middle row) 1958–1978, and (bottom row) 1958–2017.

convection in boreal summer may explain the lack of a relationship between the MJO and QBO during that season. To test this hypothesis, the potential impacts of the QBO on the vertical profile of zonal wind, temperature, and static stability are examined along the latitudes of most active MJO convection for each running 3-month average during 1979–2017. The black solid line with dots in Figure 7a indicates the latitude of highest MJO-filtered OLR variance during each season, and the dashed lines indicate latitudes 10° to the north and south. This 20° latitude band centered on the latitude of the strongest OLR variance is used to average zonal wind and temperature for the calculation of regression coefficients for each 3-month window. Figures 7b and 7c show the regression coefficients of zonal wind, temperature, and vertical temperature gradient ($\partial T/\partial p$) anomalies onto the QBO index in the upper troposphere and stratosphere.
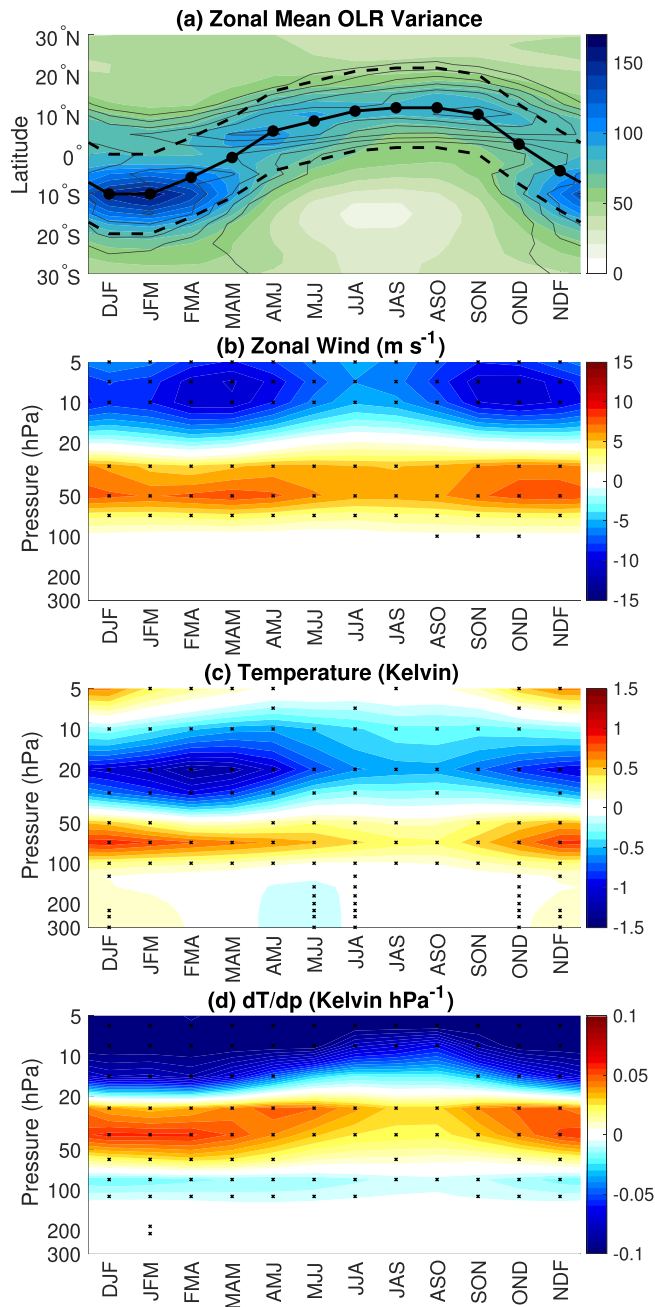
Figure 7. (a) Shading shows the climatological and zonal mean of MJO-filtered OLR variance averaged over three consecutive months centered at each month of the year (in $W^2\ m^{-4}$). Black contours show the same for total OLR variance plotted at every $100\ W^2\ m^{-4}$ intervals from $800\ W^2\ m^{-4}$ to $2,000\ W^2\ m^{-4}$. Solid black line with dots indicate the latitude of maximum MJO-filtered OLR variance. Dashed black lines indicate the latitude that is 10° north and south of the latitude of the maximum OLR variance. (b) Regression coefficients of monthly zonal wind anomalies ($m\ s^{-1}$) from 1979–2017 onto the QBO index averaged between the latitudes range bounded by dashed lines in (a). (c, d) Same as (b), except for monthly temperature anomalies (Kelvin) and their vertical gradient (Kelvin hPa^{-1}). Black dots in panels (b)–(d) indicate the regression coefficients that are statistically significantly different from zero with the 95% confidence level.

By construction, regression coefficients of zonal wind anomalies at 50 hPa are positive during all seasons at corresponding latitude bands and these are largest during the transition seasons when MJO convection is most centered around the equator (Figure 7b). A strong negative regression coefficient also appears at 7 hPa, which is consistent with the vertical scale of the QBO. Figure 7c shows substantial QBO-related changes in temperature throughout the year when following the latitude of strong MJO convection. A negative regression coefficient of $\partial T/\partial p$ in Figure 7d indicates a reduction of static stability (a positive $\partial T/\partial p$ anomaly) during easterly QBO, which appears around 100 hPa and also at 10 hPa throughout the seasons following the latitudes of convection. At 100 hPa, except around August-September-October (ASO), similar magnitudes of the regression coefficients appear during all seasons, including when the QBO-MJO relationship is weak. Therefore, the seasonal latitudinal shift in the location of MJO convection along with the change in static stability cannot on their own explain the seasonally dependent relationship between the QBO and MJO. The same conclusion can be reached by examining the longitudes of the Indo-Pacific warm pool only where the MJO convection is climatologically most active (e.g., 60–180°E).

Figure 8 compares the structure of the QBO during DJF of 1979–2017 (black solid lines) and 1958–1978 (dashed lines). The QBO index is normalized by the same standard deviation during both periods (before and after 1979), so these regression coefficients can be directly compared between the two periods. The MJO-filtered OLR variance is underestimated by JRA-55 (Figure 8a) but it captures the observed seasonal cycle (not shown). Figure 8b–d show that the amplitude of QBO zonal wind remains similar before and after 1979, but the associated temperature anomaly in the lower stratosphere is stronger during 1958–1978, which results in slightly stronger changes in upper-tropospheric lapse rate. Although Klotzbach et al. (2019) suggested that the stronger mean static stability in the upper-troposphere prior to 1980 is the reason for the non-existence of the QBO-MJO relationship, Figure 8 shows that QBO easterlies are associated with a stronger anomalous reduction of the upper-tropospheric static stability prior to 1979. Therefore, the change in the upper-tropospheric stability due to the QBO alone may not explain the absence of the QBO-MJO relationship before 1979.

Another hypothesized reason for the seasonal-dependent QBO-MJO relationship is the seasonality in the amplitude of the QBO and MJO (Nishimoto & Yoden, 2017; Son et al., 2017; Yoo & Son, 2016). Through sensitivity experiments with a cloud-resolving model, Martin et al. (2019) found that MJO convection becomes more sensitive to the QBO as its temperature anomalies increase in amplitude or decrease in height. Their result suggests that the seasonal cycle in the strength of the QBO-induced temperature could explain the seasonal-dependent QBO-MJO relationship. In addition, the MJO convection is known to be strongest during DJF (Roundy & Frank, 2004; Zhang & Dong, 2004), which may allow the MJO to interact more efficiently with the QBO during this season. However, as noted by Yoo and Son (2016), the region where MJO convection is sensitive to the QBO is zonally symmetric within the
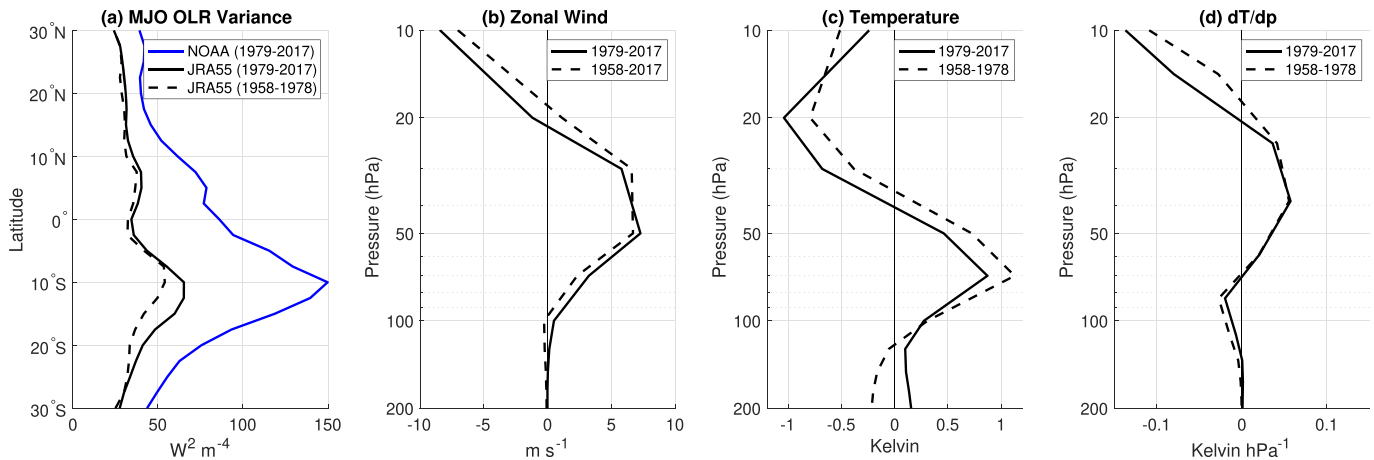
Figure 8. Same as Figure 7 except showing DJF only and comparison between the periods 1979–2017 and 1958–1978. (a) Latitudinal profile of zonal mean MJO-filtered OLR variance averaged over DJF (in $W^2 m^{-4}$) using the observed OLR from 1979–2017 (blue), JRA-55 OLR from 1979–2017 (solid black), and JRA-55 from 1958–1978 (dashed black). (b) Regression coefficients of the QBO index onto monthly zonal wind anomalies in $m \ s^{-1}$ averaged between 0° and 20°S during DJF during 1979–2017 (solid black) and 1958–1978 (dashed black). (c, d) Same as (b), except for monthly temperature anomalies (Kelvin) and their vertical gradient (Kelvin hPa^{-1}).

Indo-Pacific basin at around 5°S, not strictly following the region of climatologically active MJO convection. Furthermore, the MJO is not the only convective mode that becomes most active during DJF (Roundy & Frank, 2004). Therefore, the seasonality in MJO convective amplitude alone may not be able to explain the exclusive QBO-MJO relationship, but the seasonality in QBO amplitude may still be relevant. We further discuss the seasonality of MJO and QBO amplitudes below.

5.1. Comparison of the Vertical Structure of the MJO and CCEWs

Abhik et al. (2019) suggested that the less vertically tilted temperature anomalies in the upper troposphere and lower stratosphere associated with the MJO allow it to be more in-phase with QBO destabilization. In addition to this hypothesized mechanism by Abhik et al. (2019), we suggest that the vertical structure of the waves in the troposphere could be important to explain the present or absent relationship between them and the QBO.

Figure 9 shows the area-weighted wave phase composites of the temperature and vertical velocity profiles of each wave during 1979–2017 using all points between 15°N to 15°S and 60–180°E, where the waves are most active. As shown by Hendon and Abhik (2018), within the enhanced MJO convection (around 0° wave phase), temperature is anomalously warmer in the midtroposphere and colder at around the tropopause, which was suggested to aid the thermal destabilization caused by the QBO in the upper troposphere. However, most of anomalous cooling on the MJO time scale occurs below 100 hPa within its enhanced convective envelopes, while most of the anomalous cooling by QBO easterlies occurs above 100 hPa (Figure 8c). For the Kelvin waves, the anomalous reduction in the upper-tropospheric static stability occurs at a slightly lower altitude and does not strongly overlap with the altitude of reduced static stability by the QBO, which Abhik et al. (2019) suggested to be the reason why only a weak relationship appears between the QBO and Kelvin waves during the boreal spring. However, such an anomalous reduction in static stability in the upper troposphere is commonly seen among all waves, except that the MJO is associated with the stronger temperature anomalies in the upper troposphere than other waves.

In addition to the difference in the vertical structure of temperature, Figure 9 shows that the MJO has the most top-heavy vertical velocity profile compared to other CCEWs (Inoue et al., 2020; Sakaeda et al., 2020). Inoue et al. (2020) suggested that while a bottom-heavy profile would lead to a smaller or negative gross moist stability (Kuang, 2011; Raymond et al., 2009), a top-heavy profile indicates a greater fraction of stratiform clouds that induces anomalous column radiative warming. The top-heavy profile of the MJO vertical velocity supports the importance of cloud-radiative feedback to MJO dynamics (i.e., Del Genio et al., 2015; Sobel & Maloney, 2013; Wolding et al., 2016), and such a feedback can be enhanced when the static stability of the upper troposphere is reduced during QBO easterlies. We thus consider the possibility that convective
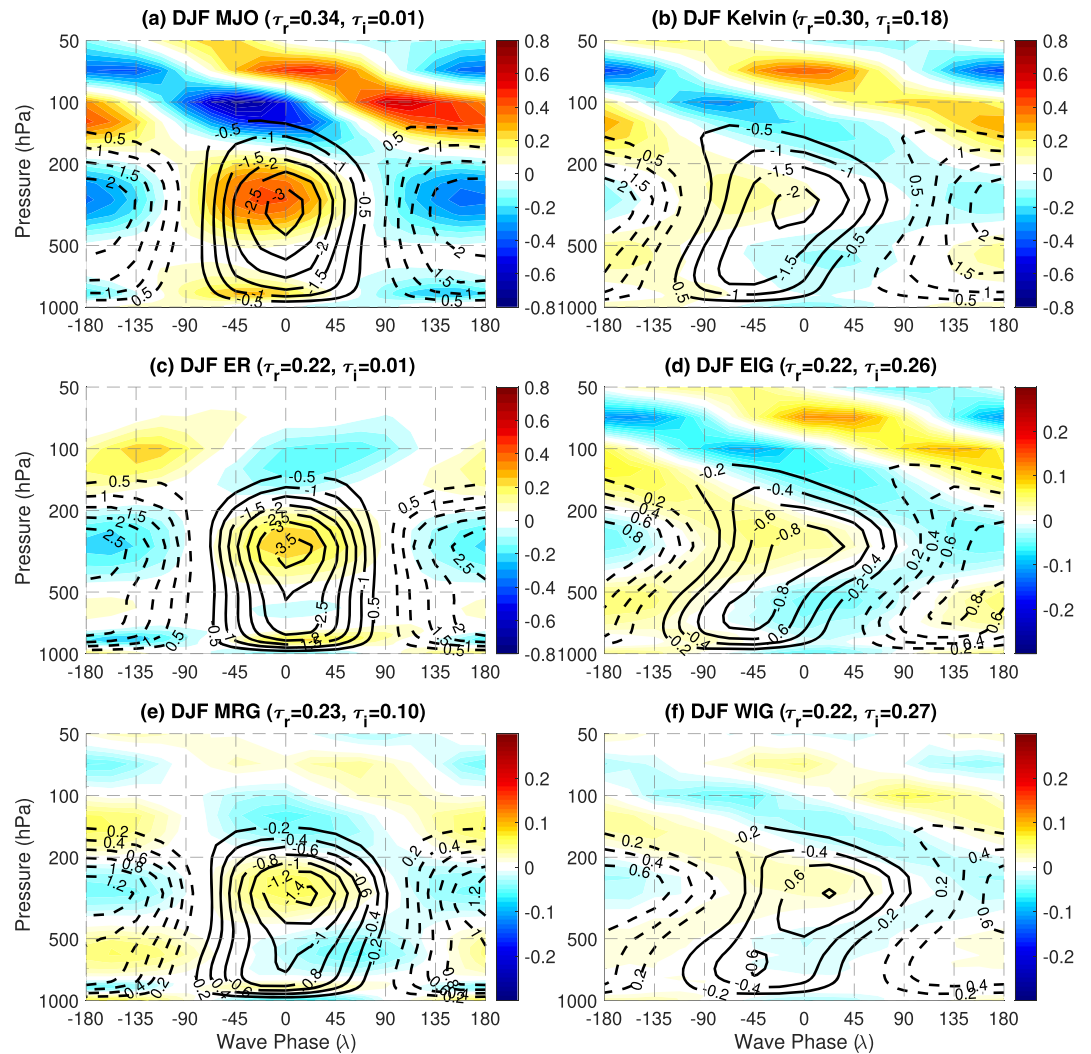
Figure 9. Wave phase (λ) and pressure diagrams of temperature (Kelvin, shaded) and vertical velocity (hPa s^{-1}, contoured) anomalies associated with the (a) MJO, (b) Kelvin, (c) ER, (d) EIG, (e) MRG, and (f) WIG waves between 15°N to 15°S and 60°E to 180°E. The values of top-heaviness τ_r and tilt ratio τ_i of the shown vertical velocity are shown in the subtitles.

modes with more top-heavy vertical velocity makes them more sensitive to the changes in the upper-tropospheric thermodynamical profiles.

To test this hypothesis, the top-heaviness of vertical motion is examined for each convective mode following the methodology introduced by Back et al. (2017). To calculate the top-heaviness of vertical velocity (ω), two leading empirical orthogonal function (EOFs) of vertical velocity profiles (Ω_1, Ω_2) are obtained using monthly mean ω between 20°N and 20°S from JRA-55. The EOFs are normalized in the same manner as in Back et al. (2017) as shown in Figure 10. The first EOF represents the first baroclinic mode associated with deep convection, while the second EOF represents the second baroclinic mode associated with stratiform rain (Schumacher et al., 2004). The two leading EOF profiles $\Omega_j(p)$ are then projected onto the wave-phase composites of vertical velocity $\hat{\omega}(p, \lambda)$ (e.g., Figure 9)

$$o_j(\lambda) = \sum^p \hat{\omega}(p, \lambda)\Omega_j(p) \qquad (2)$$

where $j = \{1, 2\}$ represents the first and second modes of vertical structure and o_j is a principal component that represents how well the composite vertical velocity $\hat{\omega}$ projects onto Ω_j with respect to the wave phase (λ).
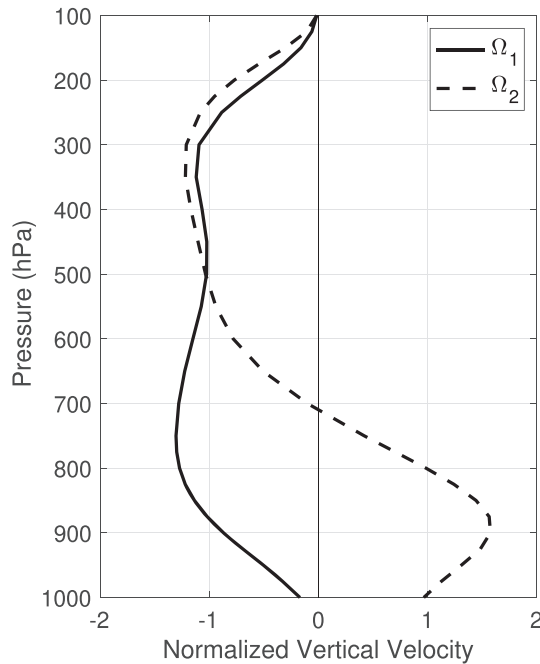
Figure 10. The normalized leading two EOF modes of JRA-55 monthly vertical velocity between 20°N and 20°S.

The top-heaviness of the waves is then estimated following the method and notation of Inoue et al. (2020). Cosine and sine waves are regressed onto the principle component o_j to find the coefficients that represent the real and imaginary components of the complex number O_j defined in Inoue et al. (2020). Then the complex parameter τ is defined as

$$\tau = \frac{O_2 O_1^*}{O_1 O_1^*} \quad (3)$$

where the asterisk indicate the complex conjugate. The real component of τ (τ_r) represents the top-heaviness and imaginary component (τ_i) indicates the tilt ratio of the vertical velocity as shown by Inoue et al. (2020).

The values of τ_r and τ_i of the wave-phase composites of vertical velocity shown in Figure 9 are indicated in the subtitles of each panel. The MJO has the highest value of τ_r and Kelvin waves has the second highest τ_r, and their values agree with Inoue et al. (2020). However, the top-heaviness of EIG, MRG, and WIG appears much higher than the ones from Inoue et al. (2020). The difference may result from the fact that our method exclusively examines the time when the waves are considered to be above noise, while such a restriction is not applied by Inoue et al. (2020). The tilt ratio of the waves agree with Inoue et al. (2020) that the lower-frequency waves such as the MJO and ER have small tilt ratios while other waves have higher ratios.

Figure 11 shows the top-heaviness τ_r of each wave calculated at each grid point during DJF. Black contours in Figure 11 show the regions above 70th, 90th, and 99th percentile of the wave-filtered OLR variance between 15°N and 15°S. Regions with small OLR variance are masked. During DJF, τ_r indicates that the MJO convection has the most top-heavy structure compared to other waves, in agreement with Figure 9. The MJO vertical velocity profile is most top-heavy around the equator between eastern Indian basin to west Pacific (Figure 11a). The geographical distribution of the top-heaviness does not have a clear relationship with the magnitude of OLR variance, suggesting that the top-heaviness and convective amplitude of the MJO are not interchangeable. Yoo and Son (2016) and Son et al. (2017) showed that the region where MJO convective activity varies with the QBO is zonally symmetric around 5°S, which is generally collocated but slightly south of the most top-heavy region and north of maximum OLR variance. The reason for this subtle geographical difference between MJO OLR amplitude, top-heaviness, and QBO sensitivity is not clear.
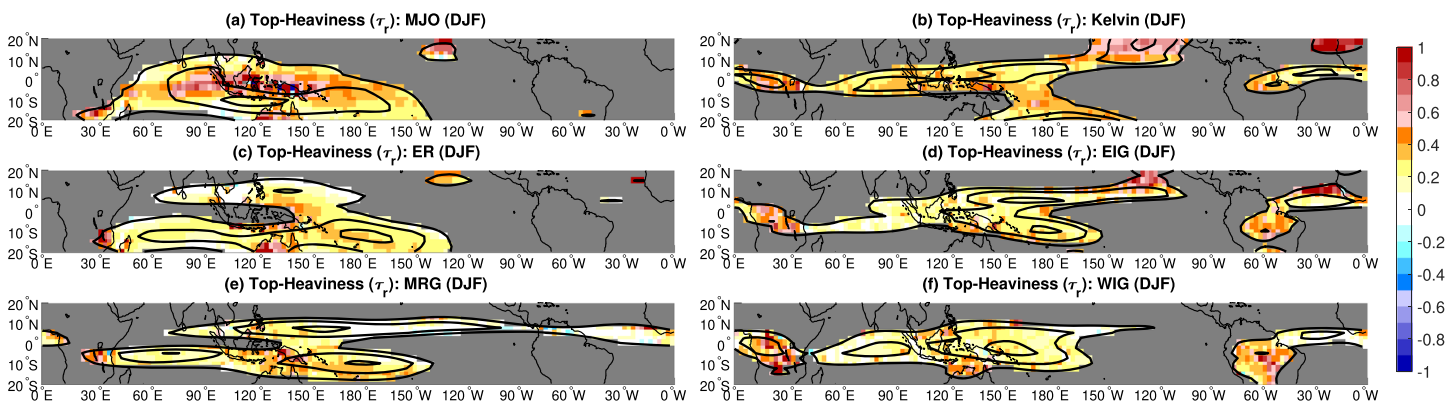

Figure 11. Shading indicates the top-heaviness of vertical velocity profile (τ_r) associated with the (a) MJO, (b) Kelvin, (c) ER, (d) EIG, (e) MRG, and (f) WIG waves during 1979–2017 DJF (see text for more details on how it is calculated). Black contours show the 70th, 90th, and 99th percentiles of the global distribution of climatological OLR variance for each wave.
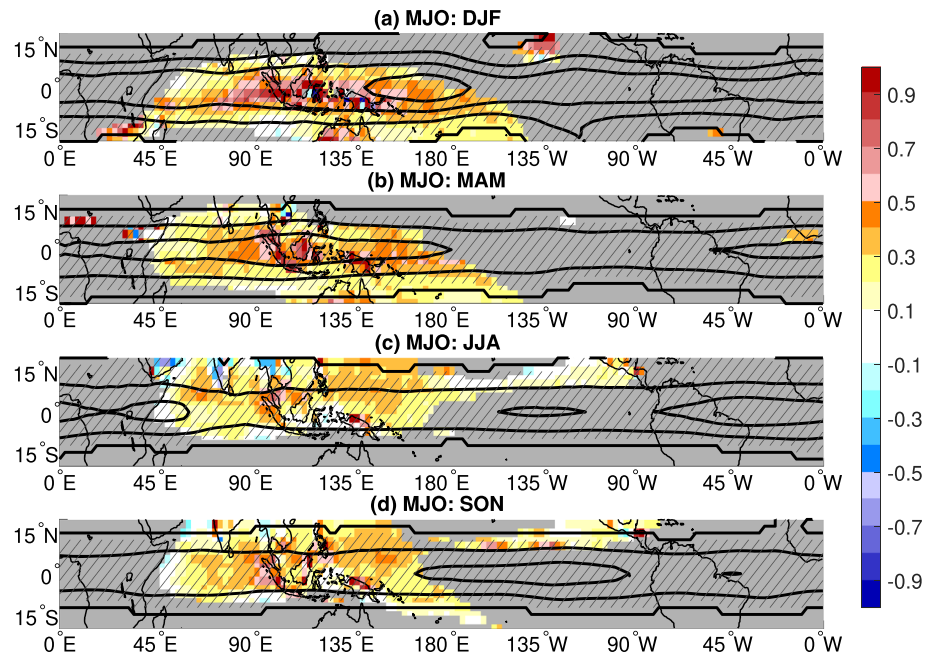
Figure 12. Shading shows the top-heaviness (τ_r) of the MJO and black contours show regression coefficients of the static stability during (a) DJF, (b) MAM, (c) JJA, and (d) SON of 1979–2017. Regression coefficients of monthly 100-hPa static stability ($\partial \hat{T} / \partial p$) against the QBO index during DJF that are plotted at every negative 0.01 K hPa^{-1} intervals from zero. Hatching indicates the region where the regression coefficients are negative. The top-heaviness is only shown where the MJO-filtered OLR variance is above the 70th percentile of its global distribution.

However, since the strongest reduction of upper-tropospheric static stability during the easterly QBO phase occurs around the equator (Densmore et al., 2019), its collocation with top-heavy profile of vertical motion may allow for the MJO to be most sensitive to the QBO.

The top-heaviness of vertical velocity may also help to explain the seasonal dependence between the MJO and QBO. Figure 12 shows τ_r for the MJO and changes in the 100-hPa static stability associated with the QBO during the four seasons. The MJO has the most top-heavy vertical profile during DJF compared to other seasons. As shown in Densmore et al. (2019), the geographical location of strongest reduction in the 100-hPa static stability associated with the QBO also changes with seasons. The reduction of static stability associated with the QBO over the Indo-Pacific basin occurs most strongly during DJF. During other seasons, weaker reductions in the static stability appear over the Indo-Pacific basin, which combined with the decreased top-heaviness of MJO vertical profile may not cause the MJO to be as sensitive to the QBO-induced changes in the static stability at the tropopause.
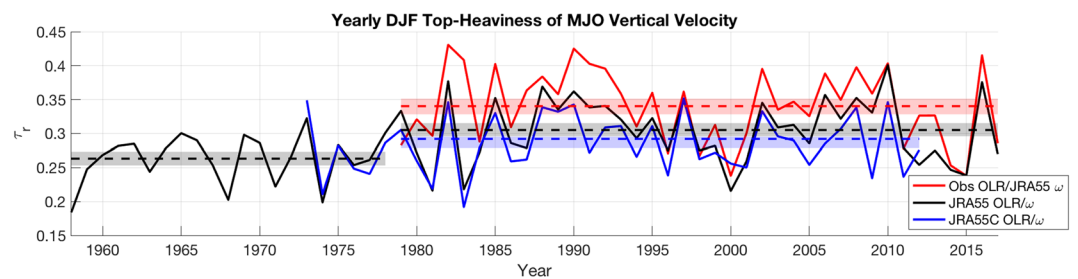

Figure 13. Yearly time series of top-heaviness of MJO vertical velocity (τ_r) during DJF that is calculated from yearly area-weighted averaged wave-phase composite of vertical velocity over 15°N to 15°S and 60°E to 180°E. Red line shows τ_r calculated using the NOAA observed OLR and JRA-55 vertical velocity (ω) after 1979, black line shows τ_r calculated using JRA-55 OLR and ω, and blue lines show τ_r calculated using JRA-55C OLR and ω. Horizontal lines show the average τ_r during 1958–1978 and 1979–2017 and its 95% confidence interval in shading.

Figure 13 shows yearly time series of area-weighted τ_r over the Indo-Pacifid basin during DJF calculated using NOAA OLR and JRA-55 data. The red line shows the top-heaviness calculated using the observed OLR and JRA-55 ω, the black line shows the value using JRA-55 OLR and ω, and the blue line shows the value using JRA-55C OLR and ω. It shows that the top-heaviness is underestimated when the MJO is detected using JRA-55 or JRA-55C OLR, but its evolution generally agrees with that using observed OLR. The horizontal dotted lines show the mean top-heaviness before and after 1979, which shows that the top-heaviness of the MJO vertical velocity is on average reduced prior to 1979. Differences in the value from JRA-55 and JRA-55C show the influence of satellite data availability. The lack of satellite data seems to result in underestimation of the top-heaviness, but the top-heaviness before 1978 is smaller than the top-heaviness after 1979 from JRA-55C. Therefore, there appears to be some reduction in the top-heaviness of the MJO before 1979, which may have contributed to the lack of its relationship with the QBO. This reduced top-heaviness of the MJO before 1979 may relate to the documented multidecadal trend in increasing MJO activity (Jones & Carvalho, 2006; Oliver & Thompson, 2013). The yearly time series of top-heaviness also correlates well with the QBO index after 1979 (significant at 95% confidence level), indicating that the top-heaviness of the MJO vertical velocity varies with the QBO, which was also shown to occur with simulated tropical deep convection (Nie & Sobel, 2015).

5.2. Cloud-Radiative Feedback of the MJO

Implication of the MJO top-heavy vertical velocity to the sensitivity of the QBO can be interpreted in a few ways. Under the assumption of the WTG and the MJO as a moisture mode (Raymond & Fuchs, 2007; Sobel et al., 2001), vertical motion is approximated as a function of diabatic heating and static stability that can influence MJO destabilization through vertical moisture advection (Chikira, 2014; Wolding et al., 2016). Therefore, one may consider the direct effect of QBO lapse rate changes on MJO vertical velocity. However, the effect of the QBO on lapse rate is mainly confined to the layer above 100-hPa (Figure 7) where the mean vertical velocity associated with the MJO does not extend into (Figure 9). Even if the vertical velocity at 100-hPa could be enhanced due to the reduction of the static stability by the QBO, moisture content is too low at this altitude to help destabilize the MJO through vertical advection. Therefore, we suggest that the top-heaviness of the vertical velocity relates to the strength of cloud-radiative feedback, another source of destabilization through reduced radiative cooling by clouds (e.g., Ciesielski et al., 2017; Del Genio et al., 2015; D. Kim et al., 2015; Lin et al., 2004; Sobel et al., 2014; B. Zhang et al., 2019). We may expect that a convective mode with a stronger cloud-radiative feedback would have stronger and more top-heavy vertical profile. Such a mode can also be more sensitive to potential changes in the strength of cloud-radiative feedback induced by the QBO. As discussed by Inoue et al. (2020), the top-heavy vertical profile of the MJO suggests that the cloud-radiative feedback plays a more important role. Adames and Kim (2016) showed that the cloud-radiative feedback is dependent on the zonal wave number within the intraseasonal time scale, it being the strongest at the planetary scale.

To check the relationship between the top-heaviness and the strength of cloud-radiative feedback, we repeat the analysis by Adames and Kim (2016) for each wave mode. The left column of Figure 14 shows the relationship between TMPA 3B42 rainfall rate and OLR anomalies filtered for each mode during DJF. Due to the unavailability of TMPA 3B42, the period of analysis is shortened to 1998–2017, during which the robust MJO-QBO relationship still appears. Shading shows the frequency of data that falls within every 2 W m^{-1} OLR and 0.2 mm hr^{-1} rainfall bins. The negative slope denotes the cloud radiative feedback parameter r defined by Adames and Kim (2016), which shows the rate of increase in anomalous longwave radiative warming with rainfall. The 95% confidence interval of the regression slope is calculated by applying bootstrap resampling of the data with a subsample size that corresponds to the degrees of freedom based on the period and zonal wave number of each wave. The cloud-radiative feedback parameter of the MJO is consistent with the result of Adames and Kim (2016) and is strongest among all wave modes. Furthermore, the radiative feedback parameter shows seasonal dependence, which becomes strongest during DJF when the MJO has the most top-heavy vertical velocity (not shown). The order of strongest to weakest cloud-radiative feedback for other waves does not seem to directly align with the top-heaviness of their vertical velocity. For example, the Kelvin wave is more top-heavy than ER and MRG waves (Figure 9) but it has weaker cloud-radiative feedback. The tilt ratio of the vertical velocity may also play a role in determining the cloud-radiative feedback parameter as it indicates the relative timing of peak convective and stratiform rain.
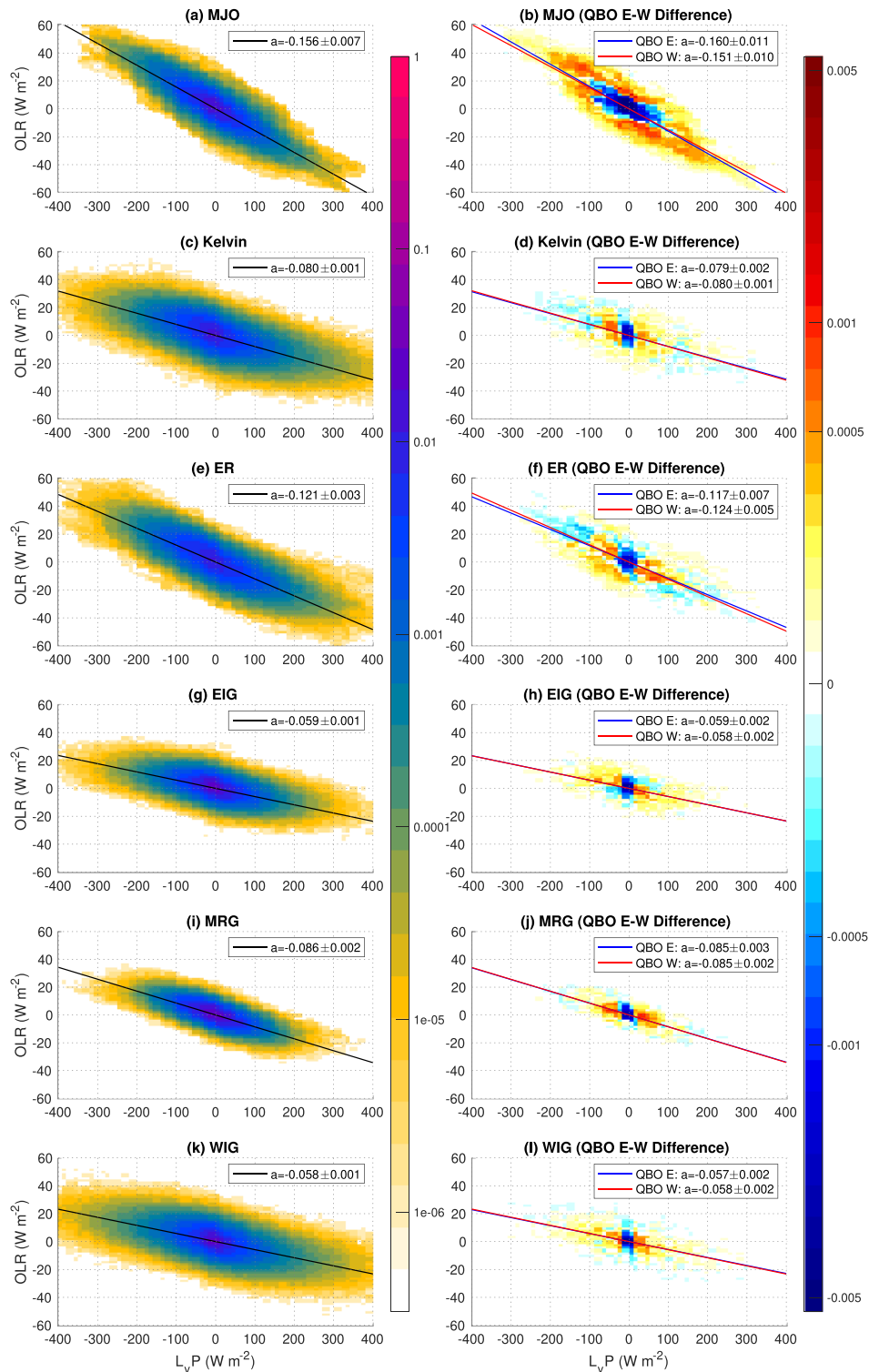
Figure 14. (left column) Shading show the distribution of wave-filtered TMPA 3B42 rainfall (P) and OLR anomalies for 0.02 mm hr^{-1} and 2 W m^{-1} bins. The rainfall on the horizontal axis is multiplied with the latent heat of vaporization (L_v). Black line shows the regression coefficients of OLR onto rainfall, which represents the cloud-radiative feedback parameter. The regression coefficients and its 95% confidence interval are shown in the legend of each panel. (right column) Shading shows the difference in the distribution between QBO easterly and westerly phases (positive indicates greater frequency during the QBO easterly). Blue and red lines show the regression coefficients during QBO easterly and westerly, respectively. Each row shows the distributions and regression coefficients for values filtered for the (a, b) MJO, (c, d) Kelvin, (e, f) ER, (g, h) EIG, (i, j) MRG, and (k, l) WIG waves.
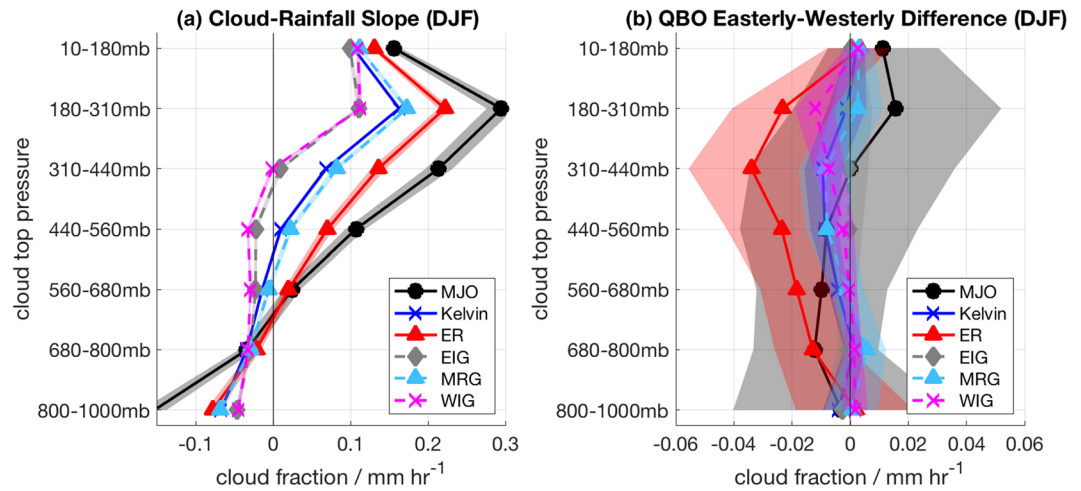
Figure 15. (a) Regression coefficients of wave-filtered ISCCP cloud fraction onto wave-filtered TMPA 3B42 rainfall for each wave. Cloud fraction is separated by the pressure of cloud top by ISCCP data. (b) Difference in the regression coefficients between QBO easterly and westerly phase. Shading around the plotted lines show the 95% confidence interval.

Further analysis of the relationship between cloud-radiative feedback and vertical structure of the waves is left for a future study, but the result confirms that the MJO has the strongest cloud-radiative feedback among the waves.

This cloud radiative feedback parameter also appears to change with the QBO. The right column of Figure 14 shows changes in the joint distribution of wave-filtered rainfall and OLR anomalies from QBO westerlies to easterlies during DJF. The magnitude of the cloud-radiative feedback parameter of the MJO increases from QBO westerly to easterly by about 6%. Although this change in the strength of cloud-radiative feedback is not statistically significant at 95% level, this result indicates that the cloud greenhouse effect is slightly stronger during the QBO easterlies, which would enhance MJO convective activity. The strength of cloud-radiative feedback prior to 1979 cannot be tested due to lack of data, but we speculate that the reduced top-heaviness of MJO vertical velocity prior to 1979 is also related to reduced strength of cloud-radiative feedback caused by the higher mean static stability around the tropopause (Klotzbach et al., 2019).

A similar analysis is repeated to compare the cloud populations associated with each wave using ISCCP cloud fraction. Cloud fractions of varying cloud-top heights are filtered for the waves and regressed onto the corresponding filtered TMPA rainfall during the period when both data are available (1998–2009). Figure 15a shows the regression coefficients, which show the rate of increase in cloud fraction with rainfall for each wave. The figure shows that the MJO is associated with the greater fraction of high clouds, which is again consistent with the top-heaviness of its vertical profile. Consistent with Figure 14b, Figure 15b shows that the MJO becomes more efficient at generating high clouds during QBO easterlies, although this is not statistically significant at 95% confidence level. In contrast, the ER and WIG appear to become less efficient at generating high clouds during QBO easterlies for reasons that are not clear, but it highlights the fact that the QBO does not influence cloudiness in the same manner for all waves. These results suggest that, during QBO easterlies, the reduced static stability or increased humidity in the upper troposphere allows the MJO to form a greater fraction of high clouds, leading to the increased cloud greenhouse effect. We suggest that the top-heavy vertical velocity reflects the degree to which the cloud-radiative feedback plays a role in the destabilization of the MJO, making it sensitive to the QBO modulation of tropopause layer lapse rate and associated cloud-radiative feedback.

6. Summary

This study first examines the unique behaviors of the relationship between the QBO and MJO. In agreement with previous results, the convective activity of the MJO tends to increase when the QBO induces easterly

wind anomalies in the lower stratosphere during the boreal winter and after around 1979 (Abhik et al., 2019; Densmore et al., 2019; Hendon & Abhik, 2018; Klotzbach et al., 2019; Nishimoto & Yoden, 2017; Son et al., 2017). Other CCEWs do not show any strong relationship with the QBO that are as robust as the boreal winter relationship between the QBO and MJO, during any season of the year. This finding is consistent with Abhik et al. (2019), but the weak relationship between the Kelvin wave and QBO found by Abhik et al. (2019) during MAM is apparently due to the strong dependence of the Kelvin wave activity on ENSO. Therefore, any hypothesis that explains the mechanism underlying the QBO-MJO relationship must be able to explain its unique relationship, seasonality, and its exclusive appearance after 1979.

Results of this study suggest that the vertical structure of a given convective mode is an important factor to determine its sensitivity to the QBO. MJO convection is shown to have the most top-heavy profile of vertical velocity compared to the CCEWs (Inoue et al., 2020). The top-heavy profile of the MJO points to an important role of cloud-radiative feedback on the destabilization of the MJO (Del Genio et al., 2015; Raymond et al., 2009; Sobel & Maloney, 2013; Wolding et al., 2016) as a more top-heavy profile generally suggests greater fraction of stratiform clouds (Back et al., 2017) that leads to a reduction of column radiative cooling. Our results confirm that the MJO is associated with the stronger cloud-radiative feedback resulting from its greater fraction of high clouds than other waves. We also find that the cloud-radiative feedback of the MJO slightly strengthens during QBO easterlies, suggesting that the reduction of the upper-tropospheric stability by the QBO leads to greater generation of high clouds. This increased efficiency of generating high clouds induces greater anomalous radiative warming, which would explain increased MJO amplitude during QBO easterlies. Therefore, the top-heaviness of vertical velocity indicates how important cloud-radiative feedback might be to the destabilization of the mode and its sensitivity to the changes in the upper-tropospheric stability by the QBO. MJO vertical velocity also becomes most top-heavy during DJF and after 1979, when the QBO-MJO relationship appears exclusively. Modeling experiments to test the sensitivity of the QBO-MJO relationship to the top-heaviness of vertical velocity would be an ideal topic for future studies.

Data Availability Statement

OLR data is available at this site (https://www.esrl.noaa.gov/psd/data/gridded/data.interp_OLR.html) and the ERA-I and JRA-55 reanalysis are available at this site (https://rda.ucar.edu/).

References

Abhik, S., Hendon, H., & Wheeler, M. (2019). On the sensitivity of convective coupled equatorial waves to the quasi biennial oscillation. *Journal of Climate*, *32*(18), 5833–5847.

Adames, Á. F., & Kim, D. (2016). The MJO as a dispersive, convectively coupled moisture wave: Theory and observations. *Journal of the Atmospheric Sciences*, *73*(3), 913–941. https://doi.org/10.1175/JAS-D-15-0170.1

Adames, A. F., Kim, D., Clark, S. K., Ming, Y., & Inoue, K. (2019). Scale analysis of moist thermodynamics in a simple model and the relationship between moisture modes and gravity waves. *Journal of the Atmospheric Sciences*, *76*(12), 3863–3881.

Back, L. E., Hansen, Z., & Handlos, Z. (2017). Estimating vertical motion profile top-heaviness: Reanalysis compared to satellite-based observations and stratiform rain fraction. *Journal of the Atmospheric Sciences*, *74*(3), 855–864.

Baldwin, M. P., Gray, L. J., Dunkerton, T. J., Hamilton, K., Haynes, P. H., Randel, W. J., et al. (2001). The quasi-biennial oscillation. *Reviews of Geophysics*, *39*(2), 179–229. https://doi.org/10.1029/1999RG000073

Boer, G. J., & Hamilton, K. (2008). QBO influence on extratropical predictive skill. *Climate Dynamics*, *31*(7), 987–1000. https://doi.org/10.1007/s00382-008-0379-5

Bretherton, C. S., & Sobel, A. H. (2003). The Gill model and the weak temperature gradient approximation. *Journal of the Atmospheric Sciences*, *60*(2), 451–460.

Butler, A., Charlton-Perez, A., Domeisen, D. I. V., Garfinkel, C., Gerber, E. P., Hitchcock, P., et al. (2019). Chapter 11 - Sub-seasonal predictability and the stratosphere. In A. W. Robertson & F. Vitart (Eds.), *Sub-seasonal to seasonal prediction* (pp. 223–241). Amsterdam, Netherlands; Oxford, UK; Cambridge, MA: Elsevier. https://doi.org/10.1016/B978-0-12-811714-9.00011-5

Chikira, M. (2014). Eastward-propagating intraseasonal oscillation represented by Chikira–Sugiyama cumulus parameterization. Part ii: Understanding moisture variation under weak temperature gradient balance. *Journal of the Atmospheric Sciences*, *71*(2), 615–639.

Ciesielski, P. E., Johnson, R. H., Jiang, X., Zhang, Y., & Xie, S. (2017). Relationships between radiation, clouds, and convection during DYNAMO. *Journal of Geophysical Research: Atmospheres*, *122*, 2529–2548. https://doi.org/10.1002/2016JD025965

Collimore, C. C., Martin, D. W., Hitchman, M. H., Huesmann, A., & Waliser, D. E. (2003). On the relationship between the QBO and tropical deep convection. *Journal of Climate*, *16*(15), 2552–2568.

Dee, D. P., Uppala, S. M., Simmons, A. J., Berrisford, P., Poli, P., Kobayashi, S., et al. (2011). The ERA-Interim reanalysis: Configuration and performance of the data assimilation system. *Quarterly Journal of the Royal Meteorological Society*, *137*, 553–597.

Del Genio, A. D., Wu, J., Wolf, A. B., Chen, Y., Yao, M.-S., & Kim, D. (2015). Constraints on cumulus parameterization from simulations of observed MJO events. *Journal of Climate*, *28*(16), 6419–6442.

Densmore, C. R., Sanabia, E. R., & Barrett, B. S. (2019). QBO influence on MJO amplitude over the maritime continent: Physical mechanisms and seasonality. *Monthly Weather Review*, *147*(1), 389–406.

Dias, J., & Kiladis, G. N. (2014). Influence of the basic state zonal flow on convectively coupled equatorial waves. *Geophysical Research Letters*, *41*, 6904–6913. https://doi.org/10.1002/2014GL061476

Dias, J., & Kiladis, G. N. (2016). The relationship between equatorial mixed Rossby-gravity and eastward inertio-gravity waves: Part II. *Journal of the Atmospheric Sciences*, *72*(5), 2147–2163.

Fritts, D. C., & Alexander, M. J. (2003). Gravity wave dynamics and effects in the middle atmosphere. *Reviews of Geophysics*, *41*(1), 1003. https://doi.org/10.1029/2001RG000106

Geller, M. A., Zhou, T., & Yuan, W. (2016). The QBO, gravity waves forced by tropical convection, and ENSO. *Journal of Geophysical Research: Atmospheres*, *121*, 8886–8895. https://doi.org/10.1002/2015JD024125

Gray, W. M., Sheaffer, J. D., & Knaff, J. A. (1992). Influence of the stratospheric QBO on ENSO variability. *Journal of the Meteorological Society of Japan. Ser. II*, *70*(5), 975–995.

Hendon, H. H., & Abhik, S. (2018). Differences in vertical structure of the Madden-Julian Oscillation associated with the quasi-biennial oscillation. *Geophysical Research Letters*, *45*, 4419–4428. https://doi.org/10.1029/2018GL077207

Hendon, H. H., Wheeler, M. C., & Zhang, C. (2007). Seasonal dependence of the MJO–ENSO relationship. *Journal of Climate*, *20*(3), 531–543. https://doi.org/10.1175/JCLI4003.1

Hodges, K. I., Chappell, D. W., Robinson, G. J., & Yang, G. (2000). An improved algorithm for generating global window brightness temperatures from multiple satellite infrared imagery. *Journal of Atmospheric and Oceanic Technology*, *17*(10), 1296–1312.

Huang, B., Banzon, V. F., Freeman, E., Lawrimore, J., Liu, W., Peterson, T. C., et al. (2015). Extended reconstructed sea surface temperature version 4 (ersst.v4). Part I: Upgrades and intercomparisons. *Journal of Climate*, *28*(3), 911–930.

Huang, P., & Huang, R. (2011). Climatology and interannual variability of convectively coupled equatorial waves activity. *Journal of Climate*, *24*(16), 4451–4465. https://doi.org/10.1175/2011JCLI4021.1

Huffman, G. J., Bolvin, D. T., Nelkin, E. J., Wolff, D. B., Adler, R. F., Gu, G., et al. (2007). The TRMM multisatellite precipitation analysis (TMPA): Quasi-global, multiyear, combined-sensor precipitation estimates at fine scales. *Journal of Hydrometeorology*, *8*(1), 38–55.

Inoue, K., Adames, A., & Yasunaga, K. (2020). Vertical velocity profiles in convectively coupled equatorial waves and MJO: New diagnoses of vertical velocity profiles in the wavenumber-frequency domain. *Journal of Atmospheric Sciences*, *77*(6), 2139–2162.

Jiang, X., Waliser, D. E., Xavier, P. K., Petch, J., Klingaman, N. P., Woolnough, S. J., et al. (2015). Vertical structure and physical processes of the Madden-Julian Oscillation: Exploring key model physics in climate simulations. *Journal of Geophysical Research: Atmospheres*, *120*, 4718–4748. https://doi.org/10.1002/2014JD022375

Jones, C., & Carvalho, L. M. V. (2006). Changes in the activity of the Madden-Julian oscillation during 1958-2004. *Journal of Climate*, *19*(24), 6353–6370. https://doi.org/10.1175/JCLI3972.1

Kessler, W. S. (2001). EOF representation of the Madden-Julian oscillation and its connection with ENSO. *Journal of Climate*, *14*, 3055–3061.

Kiladis, G. N., Wheeler, M. C., Haertel, P. T., Straub, K. H., & Roundy, P. E. (2009). Convectively coupled equatorial waves. *Reviews of Geophysics*, *47*, RG2003. https://doi.org/10.1029/2008RG000266

Kim, D., Ahn, M.-S., Kang, I.-S., & Del Genio, A. D. (2015). Role of longwave cloud-radiation feedback in the simulation of the Madden-Julian oscillation. *Journal of Climate*, *28*(17), 6979–6994.

Kim, H., Caron, J. M., Richter, J. H., & Simpson, I. R. (2020). The lack of QBO-MJO connection in CMIP6 models. *Geophysical Research Letters*, *47*, e2020GL087295. https://doi.org/10.1029/2020GL087295

Klotzbach, P., Abhik, S., Hendon, H. H., Bell, M., Lucas, C., Marshall, A. G., & Oliver, E. C. J. (2019). On the emerging relationship between the stratospheric quasi-biennial oscillation and the Madden-Julian oscillation. *Scientific Reports*, *9*(1), 2981. https://doi.org/10.1038/s41598-019-40034-6

Kobayashi, S., Ota, Y., Harada, Y., Ebita, A., Moriya, M., Onoda, H., et al. (2015). The JRA-55 reanalysis: General specifications and basic characteristics. *Journal of the Meteorological Society of Japan. Ser. II*, *93*(1), 5–48.

Kuang, Z. (2011). The wavelength dependence of the gross moist stability and the scale selection in the instability of column-integrated moist static energy. *Journal of the Atmospheric Sciences*, *68*(1), 61–74.

Lee, J.-H., Kang, M.-J., & Chun, H.-Y. (2019). Differences in the tropical convective activities at the opposite phases of the quasi-biennial oscillation. *Asia-Pacific Journal of Atmospheric Sciences*, *55*(3), 317–336.

Liebmann, B., & Smith, C. A. (1996). Description of a complete (interpolated) outgoing long-wave radiation dataset. *Bulletin of the American Meteorological Society*, *77*, 1275–1277.

Liess, S., & Geller, M. A. (2012). On the relationship between QBO and distribution of tropical deep convection. *Journal of Geophysical Research*, *117*, D03108. https://doi.org/10.1029/2011JD016317

Lim, Y., Son, S.-W., Marshall, A. G., Hendon, H. H., & Seo, K.-H. (2019). Influence of the QBO on MJO prediction skill in the subseasonal-to-seasonal prediction models. *Climate Dynamics*, *53*, 1681–1695. https://doi.org/10.1007/s00382-019-04719-y

Lin, J., Mapes, B., Zhang, M., & Newman, M. (2004). Stratiform precipitation, vertical heating profiles, and the Madden-Julian oscillation. *Journal of the Atmospheric Sciences*, *61*(3), 296–309.

Liu, C., Tian, B., Li, K.-F., Manney, G. L., Livesey, N. J., Yung, Y. L., & Waliser, D. E. (2014). Northern Hemisphere mid-winter vortex-displacement and vortex-split stratospheric sudden warmings: Influence of the Madden-Julian oscillation and quasi-biennial oscillation. *Journal of Geophysical Research: Atmospheres*, *119*, 12,599–12,620. https://doi.org/10.1002/2014JD021876

Madden, R. A., & Julian, P. R. (1994). Observations of the 40–50-day tropical oscillation. *Monthly Weather Review*, *112*, 814–837.

Marshall, A. G., Hendon, H. H., Son, S.-W., & Lim, Y. (2017). Impact of the quasi-biennial oscillation on predictability of the Madden–Julian oscillation. *Climate Dynamics*, *49*(4), 1365–1377.

Marshall, A. G., & Scaife, A. A. (2009). Impact of the QBO on surface winter climate. *Journal of Geophysical Research*, *114*, D18110. https://doi.org/10.1029/2009JD011737

Martin, Z., Wang, S., Nie, J., & Sobel, A. (2019). The impact of the QBO on MJO convection in cloud-resolving simulations. *Journal of the Atmospheric Sciences*, *76*(3), 669–688. https://doi.org/10.1175/JAS-D-18-0179.1

Nie, J., & Sobel, A. H. (2015). Responses of tropical deep convection to the QBO: Cloud-resolving simulations. *Journal of the Atmospheric Sciences*, *72*(9), 3625–3638.

Nishimoto, E., & Yoden, S. (2017). Influence of the stratospheric quasi-biennial oscillation on the Madden–Julian Oscillation during austral summer. *Journal of the Atmospheric Sciences*, *74*(4), 1105–1125.

Nishimoto, E., Yoden, S., & Bui, H.-H. (2016). Vertical momentum transports associated with moist convection and gravity waves in a minimal model of QBO-like oscillation. *Journal of the Atmospheric Sciences*, *73*(7), 2935–2957. https://doi.org/10.1175/JAS-D-15-0265.1

Oliver, E. C. J., & Thompson, K. R. (2013). A reconstruction of Madden–Julian oscillation variability from 1905 to 2008. *Journal of Climate*, *25*(6), 1996–2019.

Raymond, D. J., & Fuchs, Z. (2007). Convectively coupled gravity and moisture modes in a simple atmospheric model. *Tellus A*, *59*, 627–640.

Raymond, D. J., Sessions, S. L., Sobel, A. H., & Fuchs, Z. (2009). The mechanics of gross moist stability. *Journal of Advances in Modeling Earth Systems*, *1*, 9. https://doi.org/10.3894/JAMES.2009.1.9

Riley, E. M., Mapes, B. E., & Tulich, S. N. (2011). Clouds associated with the Madden–Julian oscillation: A new perspective from CloudSat. *Journal of the Atmospheric Sciences*, *68*(12), 3032–3051.

Rossow, W. B., & Schiffer, R. A. (1999). Advances in understanding clouds from ISCCP. *Bulletin of the American Meteorological Society*, *80*(11), 2261–2287.

Roundy, P. E., & Frank, W. M. (2004). A climatology of waves in the equatorial region. *Journal of the Atmospheric Sciences*, *61*, 2105–2132.

Sakaeda, N., Dias, J., & Kiladis, G. N. (2020). The diurnal cycle of rainfall and the convectively-coupled equatorial waves over the Maritime Continent. *Journal of Climate*, *33*(8), 3307–3331.

Sakaeda, N., Kiladis, G., & Dias, J. (2017). The diurnal cycle of tropical cloudiness and rainfall associated with the Madden-Julian oscillation. *Journal of the Atmospheric Sciences*, *30*, 3999–4020.

Scaife, A. A., Athanassiadou, M., Andrews, M., Arribas, A., Baldwin, M., Dunstone, N., et al. (2014). Predictability of the quasi-biennial oscillation and its northern winter teleconnection on seasonal to decadal timescales. *Geophysical Research Letters*, *41*, 1752–1758. https://doi.org/10.1002/2013GL059160

Schirber, S. (2015). Influence of ENSO on the QBO: Results from an ensemble of idealized simulations. *Journal of Geophysical Research: Atmospheres*, *120*, 1109–1122. https://doi.org/10.1002/2014JD022460

Schumacher, C., Houze, R. A. J., & Kraucunas, I. (2004). The tropical dynamical response to latent heating estimates derived from the TRMM precipitation radar. *Journal of the Atmospheric Sciences*, *61*(12), 1341–1358.

Sobel, A., & Maloney, E. (2013). Moisture modes and the eastward propagation of the MJO. *Journal of the Atmospheric Sciences*, *70*(1), 187–192.

Sobel, A., Nilsson, J., & Polvani, L. M. (2001). The weak temperature gradient approximation and balanced tropical moisture waves. *Journal of the Atmospheric Sciences*, *58*(23), 3650–3665.

Sobel, A., Wang, S., & Kim, D. (2014). Moist static energy budget of the MJO during DYNAMO. *Journal of the Atmospheric Sciences*, *71*(11), 4276–4291.

Son, S.-W., Lim, Y., Yoo, C., Hendon, H. H., & Kim, J. (2017). Stratospheric control of the Madden–Julian oscillation. *Journal of Climate*, *30*(6), 1909–1922.

Taguchi, M. (2010). Observed connection of the stratospheric quasibiennial oscillation with El Niño–Southern Oscillation in radiosonde data. *Journal of Geophysical Research*, *115*, D18120. https://doi.org/10.1029/2010JD014325

Wheeler, M. C., & Kiladis, G. (1999). Convectively-coupled equatorial waves: Analysis of clouds in the wavenumber-frequency domain. *Journal of the Atmospheric Sciences*, *56*, 374–399.

Wheeler, M. C., Kiladis, G. N., & Webster, P. J. (2000). Large-scale dynamical fields associated with convectively coupled equatorial waves. *Journal of the Atmospheric Sciences*, *57*(5), 613–640.

Wolding, B., Maloney, E., & Branson, M. (2016). Vertically resolved weak temperature gradient analysis of the Madden-Julian Oscillation in SP-CESM. *Journal of Advances in Modeling Earth Systems*, *8*, 1586–1619. https://doi.org/10.1002/2016MS000724

Wolding, B., Maloney, E., Henderson, S., & Branson, M. (2017). Climate change and the Madden-Julian oscillation: A vertically resolved weak temperature gradient analysis. *Journal of Advances in Modeling Earth Systems*, *9*, 307–331. https://doi.org/10.1002/2016MS000843

Xu, J.-S. (1992). On the relationship between the stratospheric quasi-biennial oscillation and the tropospheric southern oscillation. *Journal of the Atmospheric Sciences*, *49*(9), 725–734.

Yasunaga, K., & Mapes, B. (2011). Differences between more divergent and more rotational types of convectively coupled equatorial waves. Part I: Space–time spectral analyses. *Journal of the Atmospheric Sciences*, *69*(1), 3–16.

Yasunaga, K., & Mapes, B. (2013). Differences between faster versus slower components of convectively coupled equatorial waves. *Journal of the Atmospheric Sciences*, *71*(1), 98–111. Retrieved from http://doi.org/10.1175/JAS-D-13-03.1

Yoo, C., & Son, S.-W. (2016). Modulation of the boreal wintertime Madden-Julian oscillation by the stratospheric quasi-biennial oscillation. *Geophysical Research Letters*, *43*, 1392–1398. https://doi.org/10.1002/2016GL067762

Zhang, C. (2005). Madden-Julian oscillation. *Reviews of Geophysics*, *43*, RG2003. https://doi.org/10.1029/2004RG000158

Zhang, C., & Dong, M. (2004). Seasonality in the Madden–Julian Oscillation. *Journal of Climate*, *17*(16), 3169–3180.

Zhang, B., Kramer, R. J., & Soden, B. J. (2019). Radiative feedbacks associated with the Madden-Julian oscillation. *Journal of Climate*, *32*(20), 7055–7065. Retrieved from https://doi.org/10.1175/JCLI-D-19

Zhang, C., & Zhang, B. (2018). QBO-MJO connection. *Journal of Geophysical Research: Atmospheres*, *123*, 2957–2967. https://doi.org/10.1002/2017JD028171